LANDAU THEORY OF COMPLEX ORDERED PHASES

LANDAU THEORY OF COMPLEX ORDERED PHASES

By Duncan McClenagan, B. Sc. (Honours)

A Thesis Submitted to the School of Graduate Studies in Partial Fulfillment of the Requirements for the Degree of Master of Science

McMaster University

McMaster University

MASTER OF SCIENCE (2019)

Hamilton, Ontario (Physics & Astronomy)

TITLE: Landau Theory of Complex Ordered Phases

AUTHOR: Duncan McClenagan, B. Sc. (Honours)

SUPERVISOR: Professor An-Chang Shi

NUMBER OF PAGES: xii, 84

Lay Abstract

Soft condensed matter physics studies the properties of materials that easily deform, such as soap, gel and plastic. Many of these materials can self-assemble into various fascinating ordered structures. One particularly complex class of structures, found in a wide range of soft materials, is the class of Frank-Kasper phases. Frank-Kasper phases in soft materials have potential applications in fields such as photonics, so their formation in these materials is particularly interesting. However, it is not well understood why the Frank-Kasper structures occur in so many soft materials. We investigate this problem, and show that the occurrence of these structures might be described by a very simple mathematical model known as the Landau-Brazovskii model. The fact that such a simple model can predict the complex Frank-Kasper phases provides insight into the origin of the widespread nature of the occurrence of Frank-Kasper phases in soft materials.

Abstract

Recently, a number of spherical packing phases belonging to the class of Frank-Kasper (F-K) phases have been observed in a wide range of soft matter systems, including block copolymers, ionic surfactants, liquid crystalline dendrimers, and giant surfactants. Although their emergence in such systems has been conjectured to be due to a competition between mesodomain sphericity and incompressibility, we lack a description of a precise and general mechanism underlying the formation of F-K phases in soft matter systems. In this work, we consider the two most common F-K phases found in soft matter systems, the σ and A15 phases, and study their stability in the context of a well-known Landau model known as the Landau-Brazovskii model. This model has been applied to systems ranging from block copolymers to liquid crystals. We find that the phase behavior of the Landau-Brazovskii model is controlled only by two parameters, rather than by three parameters, as was suggested by previous works. We also find that the Landau-Brazovksii phase diagram contains regions in which the σ or A15 phase is the most stable among a set of candidate phases. The fact that such a simple model can predict these complex phases provides some insight into the question of why the occurrence of the Frank-Kasper phases in soft matter is so widespread.

Acknowledgments

I would like to thank my supervisor, Dr. An-Chang Shi, for his patience, input, and support. I would also like to thank Dr. Kai Jiang, who performed calculations to help verify our results. I thank my supervisory/examination committee for the time spent in committee meetings and in reading my thesis. I also thank my colleague, Tom Lai, for support and input. Furthermore, I should note that the funding for this work was provided by the Natural Sciences and Engineering Research Council, the Government of Ontario, the A. Boyd McLay Ontario Graduate Scholarship, my supervisor, and McMaster University.

Contents

List of Figures

List of Tables

Declaration of Academic Achievement

The main result of this thesis – the phase diagram presented in Fig. 3.1 – is a result of calculations conducted by me. The thesis was written entirely by me, and edited by my supervisor, Dr. An-Chang Shi, and by me. My colleague, Tom Lai, also provided some input regarding an early draft of the thesis. Dr. Kai Jiang performed calculations to verify our initial results. Dr. Shi was the source of most of the theoretical ideas which led to the main results of this thesis. Dr. Shi also provided much additional input and assistance.

Chapter 1

Introduction

Soft condensed matter physics studies the properties of materials which are relatively easy to deform at room temperature [1–3]. The domain of soft matter physics includes polymeric systems, colloids, surfactant suspensions, and even biological systems [1, 3]. These soft matter systems, often simply called "soft matter," are usually composed of basic constituent units, such as polymers or colloidal particles, which are very large compared to atomic length scales [1–3]. Soft matter commonly exhibits complex behavior both at and/or out of equilibrium. These systems frequently contain multiple intrinsic length scales [1], and often produce nonlinear responses to external perturbations [1, 2]. The diverse, interesting behavior and many applications of soft matter make its study an attractive proposition, and the field has been growing in recent years.

Given the right conditions, soft matter systems can form a wide array of mesoscopic ordered structures [1], sometimes similar to those formed in conventional metallic crystals [4]. We will focus on a problem related to the self-assembly of these structures; in particular, our topic relates to the spontaneous and somewhat unexpected emergence of certain particularly complex structures in a wide range of soft matter systems.

1.1 Self-Assembly in Soft Matter

In soft matter physics, the characteristic binding energy between constituent units is typically similar in magnitude to the characteristic room temperature thermal energy $k_B T$ [2, 3]. Hence, entropy frequently plays an important role in soft matter [2].[1]

The competition between entropic and energetic effects can cause soft matter systems to self-assemble into ordered one-, two-, and three-dimensional structures [1, 4–6]. Many of these structures are similar to those found in more traditional atomic crystal systems [4], where the “atoms” in metallic systems correspond to macromolecular clusters of molecules in soft systems. For instance, the phase diagram of AB diblock copolymers exhibits a generic phase transition sequence from the lamellar phase (a one-dimensional phase consisting of periodic sheets), to a bicontinuous network phase (the double gyroid phase), to the cylindrical hexagonal phase (consisting of cylinders packed on a hexagonal lattice), to the BCC (body-centered cubic) phase (consisting of

---

[1] When the characteristic binding energy per constituent unit ϵ is similar in magnitude to the characteristic thermal energy per constituent unit $k_B T$, each constituent unit has considerable freedom to move around and explore its phase space, and this exploration is controlled by the tendency to maximize entropy.

spheres packed on a BCC lattice), and finally to the HCP (hexagonally close packed) phase (consisting of spheres on an HCP lattice), as the volume fraction f_A of the minority A-blocks decreases from $f_A = \frac{1}{2}$ [7]. The aforementioned structures (schematic depictions of which are shown in Fig. 1.1) are comprised of polymeric domains rich in the monomers of one particular block type (usually the type of block with the smaller volume fraction), which sit in a matrix of monomers of the other block type. For instance, in a body-centered cubic phase, the spheres are usually rich in monomers of the type with the smaller volume fraction.

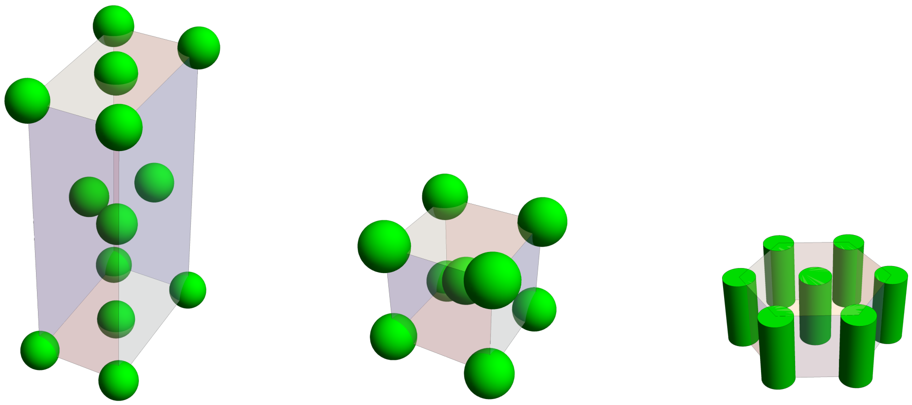

(a) HCP unit cell (b) BCC unit cell (c) Cylindrical hexagonal structure

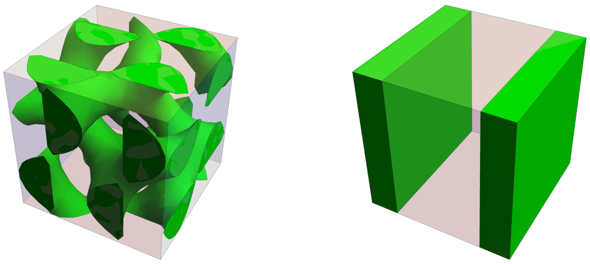

(d) Double gyroid unit cell (e) Lamellar structure

Figure 1.1: Some structures (one-, two-, and three-dimensional) found in soft matter systems.

In recent years, certain members of a complex class of structures known as the Frank-Kasper phases have been found in a wide range of soft matter systems, including liquid-crystalline systems [8–10], small ionic surfactants [6], block copolymer melts [11–15], nanoparticle mixtures [16], and in certain hybrid macromolecules, such as so-called “giant tetrahedra” and “giant surfactants” [5]. The Frank-Kasper phases were originally discovered over 60 years ago in metallic alloys [17–19], but their discovery in these soft matter systems occurred mostly in recent decades. The existence of Frank-Kasper phases in metallic alloys is, perhaps, to be expected, as Frank-Kasper phases always contain at least two types of non-equivalent lattice sites, making them natural candidates for systems with more than one type of constituent unit. However, in soft condensed matter, Frank-Kasper phases are often formed such that the macromolecular “atoms” in the system are made only of *one* type of constituent unit (e.g., one type of monomer in a block copolymer system) [5, 6, 8–12, 14], in contrast to their original discovery in multi-component metallic systems. Indeed, even now, most known metallic systems for which a Frank-Kasper phase is stable are multi-component systems, two exceptions being uranium and manganese [12]. The exact mechanisms governing the appearance of these phases in soft systems are not yet fully understood.

In this thesis, I shall show how we produced a phase diagram of a well-known Landau free energy functional, and shall discuss the existence of two important Frank-Kasper phases within this diagram. The existence of these Frank-Kasper phases in the aforementioned phase diagram provides some insight into the universality of the appearance of Frank-Kasper phases in soft systems.

1.2 The Frank-Kasper Phases

1.2.1 Origin and Significance

Even in physics, it often pays to start with history. The class of Frank-Kasper phases was originally constructed over 60 years ago by Sir Charles Frank and J. S. Kasper, who used these phases to model certain metallic alloys [17, 18]. In one of two seminal papers on the topic, Frank and Kasper noted that certain transition metal alloys exhibit complex crystal structures formed by piecing together four distinct types of coordination polyhedra[2] with 12, 14, 15, and 16 vertices.

Now, at sufficiently high pressure or with sufficiently strong interparticle attractive potentials, it is natural to suppose that packing efficiency – how many atoms, or other constituent units, one can fit in a unit volume – plays an important role in determining the equilibrium structures of a system. Assuming that we can model some system as a collection of hard spheres, the packing fraction of the spheres (the spatial volume fraction occupied by the spheres) will be an important factor in determining the equilibrium ordered phases of the system. Indeed, the fact that the maximum equal-volume hard sphere packing fraction of $\frac{\pi}{\sqrt{18}} \approx 0.74$ (this packing fraction has been thought to be the maximum since

---

[2] If one considers a single, central atom in such a structure, the centers of the surrounding neighbouring atoms can be joined to form a polyhedron. It is this that I refer to by the term "coordination polyhedron." Here I employ the definition of "neighbours" used by Frank and Kasper, in which a "neighbour" is any atom which is the first to be encountered as one proceeds in a straight line from the central atom through the Voronoi cell of this atom, in such a way as to make this line intersect the Voronoi cell normally to the planar face being pierced.

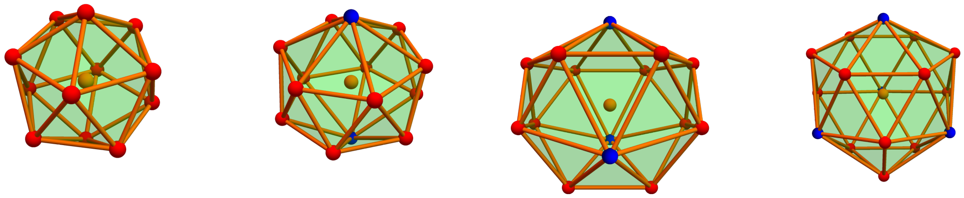

(a) CN-12 (icosahedron) – I_h

(b) CN-14 – D_{6d}

(c) CN-15 – D_{3h}

(d) CN-16 – T_d

Figure 1.2: Sample Frank-Kasper coordination polyhedra of each of the four types (CN = coordination number). The central atoms are colored yellow, and the coordination atoms are coloured according to the number of coordination polyhedron edges to which they are connected: coordination atoms connected to five edges are coloured red, and coordination atoms connected to six edges are coloured blue. The ideal point group symmetries of each polyhedron are also given (see [20, 21]).

at least 1611, when Kepler made such a conjecture, but this was not proven until 1998 [22]) is attained with the FCC and HCP lattices [22, 23] has been invoked to explain the prevalence of the HCP structure in a variety of hard and soft materials [23]. Noting the importance of sphere-packing in determining the favored structures in complex materials, Frank and Kasper [17] proceeded to consider the local grouping of 12 spherical coordination atoms and one central spherical atom. This is a natural grouping to consider, because (assuming equal-volume coordination spheres) “12” is the maximum number of spheres that can be placed in contact with a central sphere of the same size, and, as mentioned, tight packing is often preferred in crystal systems. We then ask the question: what is the best way to arrange the 12 coordination atoms around the central atom; in other words, what is the preferred coordination geometry?

If we assume that all spheres in our local grouping are of equal volume, and if we assume that the spheres associated with the coordination atoms all contact the central sphere – which is a natural assumption to make since we are considering tightly packed configurations – then there are only three possible coordination geometries. One possibility is icosahedral coordination, where the 12 coordination atoms sit on the vertices of an icosahedron. The only other possible coordination environments are those associated with the FCC and HCP lattices [17]. Again, considering the equal-sphere-volume case, the FCC, HCP, and icosahedral coordination environments all lead to the same local packing density (that is, the radius of the smallest encompassing sphere is the same [17]). However, if the spheres are slightly deformable, icosahedral coordination can have advantages over the FCC and HCP coordination types.

First, if the spheres are not truly hard spheres, but are mutually attracting, deformable, "soft spheres" interacting via a Lennard-Jones potential, then the local grouping of 13 atoms can achieve a higher binding energy with icosahedral coordination than it can with the FCC and HCP coordination environments [17, 24]. This results from the fact that, in contrast to the case of FCC or HCP coordination, it is not necessary (even if all spheres have the same volume) for the coordination spheres in an icosahedral coordination environment to touch each other, allowing for more freedom in deformation [17]. This suggests that icosahedral coordination produces more favourable local packing in systems of mutually attracting, deformable "soft" spheres [17].

Secondly, the fact that there are many possible (non-regular) icosahedral coordination environments allows one to select an environment that accommodates a set of coordination atoms with slightly different radii [17] – one cannot do this as easily with FCC or HCP coordination, because in such coordination environments all atoms in the coordination shell touch one another (if the coordination atoms have the same size as the central atom), and therefore one would have to enlarge the central atom in order to enlarge any atom on the coordination shell. Therefore, one might expect icosahedral coordination to be locally preferred by systems with multiple types of atoms.

These two advantages might suggest that there should be many cyrstalline materials, especially those with multiple atom types, which contain icosahedral coordination within their ordered phases. Unfortunately, icosahedra cannot fill space due to their crystallographically-forbidden five-fold symmetry. In order to efficiently fill space, it is necessary to supplement icosahedra with other coordination polyhedra. This is how the Frank-Kasper phases are constructed: one supplements 12-vertex distorted icosahedra with 14-, 15-, and/or 16-vertex polyhedra [17] (see Fig. 1.2), the larger polyhedra being natural locations for larger atoms in a multi-component system. The 14-, 15-, and 16-vertex polyhedra are chosen so that all faces are triangular, and so that every vertex in such a polyhedron is attached to either five or six edges, and, finally, so that no two vertices connected to six edges (each) themselves share an edge [17, 20]. There are no polyhedra with a vertex count different than 12, 14, 15, or 16 that meet all the criteria above [17, 20] (the 12-vertex polyhedron meeting these criteria is the icosahedron). I will refer the reader to [17] for the reasoning underlying these criteria. It should be noted, however, that because each of these polyhedra (including the icosahedron) is constructed in such a way that every face is triangular [17], when combined these coordination polyhedra yield a structure in which all interstices in the system are tetrahedral (which gives the Frank-Kasper phases the alternate name “tetrahedrally close-packed”

[tcp] phases). The (nearly regular [4]) tetrahedral nature of the interstices can be partially rationalized by noting that a regular tetrahedron represents the densest local packing for a group of four equal-sized spheres [4, 17].

One can form a large array of Frank-Kasper phases from the four coordination polyhedra mentioned above. To my knowledge, 27 types of Frank-Kasper phases have been observed in physical systems [20]; it is possible, however, to construct a number of additional Frank-Kasper structures which are not among these 27 observed types [20]. The Frank-Kasper phases have been discovered in many intermetallic elements [12], including superconductors like Nb_3Zr [25] and Nb_3Sn [25, 26]. However, our concern is the existence of these phases in soft matter systems.

1.2.2 Soft Matter Systems

Recently, a number of Frank-Kasper phases (including the A15 [5, 6, 10, 14], σ [5, 6, 8, 9, 11, 12], C14 [13, 27], and C15 [13, 27] structures) have been observed in soft condensed matter systems. As mentioned in §1.1, many soft matter systems form Frank-Kasper phases in which the spherical domains (the macromolecular analogous of the atoms in metallic crystal systems) consist of only one species of molecule or macromolecule. The single-component nature of the domains in these materials stands in contrast to the metallic case, where Frank-Kasper phases mainly exist in alloys. The principles underlying this type of Frank-Kasper phase formation are not, to our knowlege, completely understood. In this work, we will focus on two Frank-Kasper phases, the A15 and σ phases, which represent the most common Frank-Kasper phases found in soft matter systems [5].

σ and A15 Phases

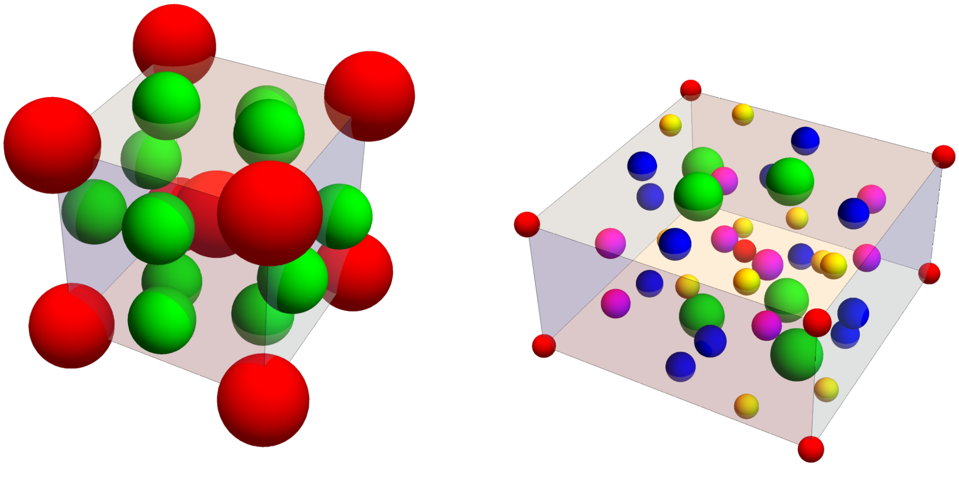

(a) A15 unit cell

(b) σ unit cell

Figure 1.3: Schematic depictions of σ and A15 unit cells. The atoms are coloured according to which of the (nonequivalent) types of lattice sites they occupy. The parameters used to generate the σ unit cell depiction are found in [28].

The A15 phase (space group: $Pm\overline{3}n$) is a cubic phase with two nonequivalent types of lattice sites: one whose atoms sit at the edges and center of the conventional unit cell, and one whose atoms are placed (two at a time, at equal distances from the nearest edge and from each other) along lines subdividing the cubic faces into two congruent parts [21] (see Fig. 1.3a). The atoms on the faces have an icosahedral coordination shell with a coordination number of 12; the central and corner atoms have a coordination number of 14 [21, 29]. The A15 phase is found in a number of transition metal alloys, including IrV_3,

Cr_3Si, and $AlNb_3$ [21]. It has also been identified experimentally in a number of soft matter systems, including diblock copolymer melts [14], tetrablock copolymer melts [15], giant surfactants [5], giant tetrahedra [5], ionic surfactants [6], and dendrimers [5, 10]. More details on the A15 structure are found in §A.1.

The σ phase (space group: $P4_2/mnm$) has a larger, much more complicated tetragonal unit cell with 30 atoms (Fig. 1.3b) [5]. In this unit cell, there are five non-equivalent types of lattice sites [21]. Two of them have 12-fold coordination, two have 14-fold coordination, and one has 15-fold coordination [21, 29]. See §A.2 for details. The σ phase has been identified in metallic alloys, such as CrFe, FeMo, and $AlNb_2$ [21]. It has also been found in a number of soft systems, including diblock and tetrablock copolymers [11, 15], dendrimers [8, 9], giant surfactants [5], and ionic surfactants [6].

Formation Mechanisms of Frank-Kasper Phases in Soft Matter

The reasons for the occurrence of the Frank-Kasper phases in such a diverse array of soft systems are currently unclear. Nevertheless, one important factor contributing to the formation of these phases appears to be the existence of competition between the tendency of soft systems to fill space without gaps[3] and the tendency of such systems to form spherical minority domains (this last tendency can be rationalized by noting that sphericity minimizes interfacial area costs per unit volume) [4]. Although we are focusing on soft matter, it is interesting to note that a similar mechanism – competition between packing

---

[3] This tendency, favoured by attractive van der Waals forces [23], is similar to the tendency of hard crystalline systems to adopt ordered structures with high spherical packing fractions.

considerations and a tendency towards maximum Jones zone sphericity – has been proposed [12, 30] to explain the existence of Frank-Kasper phases in certain metallic systems.

The stability of the σ and A15 phases in diblock copolymer melts, for instance, has been explained as follows. Define the isoperimetric quotient of a closed three-dimensional region $\mathcal{R}$ in real space by $\mathcal{S}\left(\mathcal{R}\right) = 36\pi[V(\mathcal{R})]^2/[A(\mathcal{R})]^3$, where A is the surface area of $\mathcal{R}$ and V is its volume [7]. It is easy to verify that $\mathcal{S}$ is simply the cube of the ratio between the surface area of a sphere with the same volume as $\mathcal{R}$ and the surface area of $\mathcal{R}$ itself. Hence, $\mathcal{S}$ is a measure of how much $\mathcal{R}$ deviates from a sphere of the same volume. Since the sphere is the minimal surface-area region at any given volume, $\mathcal{S}$ is bounded above by unity. With this definition in place, one can make the following argument (see [7]). For a diblock copolymer melt in an ordered three-dimensional phase (the BCC phase, for instance), under suitable conditions one might expect the (roughly) spherical minority domains in the system to deform to approximately match the shape of the Voronoi cells associated with the lattice sites upon which they sit. This is intuitively reasonable, because block copolymer melts are incompressible, and there exists within them an entropic tendency to avoid excessive stretching or compression of their polymers. Now, there exists some free energy cost of the interfacial surface between any minority domain (rich in one particular block type) in the system and the surrounding matrix (rich in the other block type), due to chemical incompatibility between the two block types. Hence, one expects the system to prefer to form spherical minority domains if possible, in order to minimize this interfacial cost.

However, the shape of the domain is constrained also by its tendency to match the shape of its surrounding Voronoi cell. One might, therefore, expect the system to prefer structures whose Voronoi cells have, on average, high sphericities (that is, high $\mathcal{S}$-values). In this way, the system could simultaneously form highly spherical domains while adopting minority domain shapes that approximately match those of the enclosing Voronoi cells. If one computes the average Voronoi cell $\mathcal{S}$-values for the "classical" FCC and BCC structures, along with those for the A15 and σ phases, for instance, one finds that the σ and A15 phases typically have very close average $\mathcal{S}$-values (0.7617(0) and 0.7617(4), respectively[4] [7]) which are both considerably higher than those for the FCC and BCC phases (0.7405 and 0.7534, respectively [7]). This fact has been proposed to explain the preference in diblock copolymer melts (under certain conditions) of the σ and A15 phases over the more common spherical FCC and BCC structures [7] (see also [4, 11, 12] for similar arguments).

Unfortunately, a general theory of Frank-Kasper phase formation in soft matter systems does not yet, to my knowledge, exist, although considerable progress in this area has been made in the context of block copolymer systems [4, 7, 12, 19, 31, 32]. We wished to gain a better understanding of the general principles governing the soft matter formation of Frank-Kasper phases in general, and of the σ and A15 phases in particular. To do so, we examined the phase behavior of a generic Landau model known as the Landau-Brazovskii model.

---

[4] For the σ phase, the average value of $\mathcal{S}$ depends on the ratio of the two non-equal lengths of the σ phase unit cell. We are assuming a typical value for this ratio of 1.89 [7].

1.3 Landau-Brazovskii Model

The Landau-Brazovskii model [33–36] is a generic model for describing weakly first-order order-disorder phase transitions for isotropic systems (that is, systems for which the free energy, as a function of some order parameter field, is invariant under spatial rotations) whose equilibrium order parameter fields are dominated in Fourier space by a single, finite principal wavenumber q_0. This model has been applied to a variety of specific physical systems, including block copolymers [35, 37, 38] and liquid crystals [34]. The model has also been derived for more general systems of hard spheres interacting via an isotropic pairwise potential which is either short-ranged or strongly negatively peaked in Fourier space [39]. A generalization of the Landau-Brazovskii model has been applied to a wide range of other microphase-separating systems [40].

The Landau-Brazovskii functional can be derived in a straightforward manner. First, one performs a Taylor expansion of the free energy $\tilde{F}$ in the order parameter field $\tilde{\phi}\left(\tilde{\mathbf{r}}\right)$, truncating this expansion at the fourth-order term:

$$\begin{aligned}\tilde{F}\left[\tilde{\phi}\left(\tilde{\mathbf{r}}\right)\right] = \tilde{F}_0 \;+\; & \int_{\tilde{\Delta}\times\tilde{\Delta}} \gamma_2\left(\tilde{\mathbf{r}}_1,\tilde{\mathbf{r}}_2\right)\tilde{\phi}\left(\tilde{\mathbf{r}}_1\right)\tilde{\phi}\left(\tilde{\mathbf{r}}_2\right)\;\mathrm{d}^3\tilde{\mathbf{r}}_1\mathrm{d}^3\tilde{\mathbf{r}}_2 \\ + & \int_{\tilde{\Delta}^3} \gamma_3\left(\tilde{\mathbf{r}}_1,\tilde{\mathbf{r}}_2,\tilde{\mathbf{r}}_3\right)\tilde{\phi}\left(\tilde{\mathbf{r}}_1\right)\tilde{\phi}\left(\tilde{\mathbf{r}}_2\right)\tilde{\phi}\left(\tilde{\mathbf{r}}_3\right)\;\mathrm{d}^3\tilde{\mathbf{r}}_1\mathrm{d}^3\tilde{\mathbf{r}}_2\mathrm{d}^3\tilde{\mathbf{r}}_3 \\ + & \int_{\tilde{\Delta}^4} \gamma_4\left(\tilde{\mathbf{r}}_1,\tilde{\mathbf{r}}_2,\tilde{\mathbf{r}}_3,\tilde{\mathbf{r}}_4\right)\tilde{\phi}\left(\tilde{\mathbf{r}}_1\right)\tilde{\phi}\left(\tilde{\mathbf{r}}_2\right)\tilde{\phi}\left(\tilde{\mathbf{r}}_3\right)\tilde{\phi}\left(\tilde{\mathbf{r}}_4\right)\;\mathrm{d}^3\tilde{\mathbf{r}}_1\mathrm{d}^3\tilde{\mathbf{r}}_2\mathrm{d}^3\tilde{\mathbf{r}}_3\mathrm{d}^3\tilde{\mathbf{r}}_4,\end{aligned}$$

where $\tilde{\Delta}$ is the spatial domain of the system. The Landau-Brazovskii model simplifies the expansion by approximating the third- and fourth-order terms as local terms. This model also rewrites the second-order term in Fourier space, where it can be written as an integral over a single wavevector because of translational symmetry. Then, by approximating the second order coefficient with a quadratic expression centered on the principal wavenumber q_0, and choosing $\tilde{F}_0 = 0$, we arrive at the Landau-Brazovskii free energy functional [36]:

$$\tilde{F}\left[\tilde{\phi}\left(\tilde{\mathbf{r}}\right)\right] = \int_{\tilde{\Delta}} \mathrm{d}^3\tilde{\mathbf{r}} \left[\frac{\tilde{\xi}^2}{8{q_0}^2}\left(\nabla^2\tilde{\phi} + {q_0}^2\tilde{\phi}\right)^2 + \frac{\tilde{\tau}}{2}\tilde{\phi}^2 - \frac{\tilde{\gamma}}{3!}\tilde{\phi}^3 + \frac{\tilde{\lambda}}{4!}\tilde{\phi}^4\right], \tag{1.1}$$

where $\tilde{\phi}\left(\tilde{\mathbf{r}}\right)$ is the order parameter field as a function of position $\tilde{\mathbf{r}}$, and $\tilde{\xi}$, $\tilde{\tau}$, the symmetry parameter $\tilde{\gamma}$, and $\tilde{\lambda} > 0$ are adjustable parameters. Note that $\tilde{F}$ is invariant under the transformation $\tilde{\phi} \to -\tilde{\phi}, \tilde{\gamma} \to -\tilde{\gamma}$.

By re-scaling the free energy, position variable, and order parameter field, we can reduce the number of parameters in the Landau-Brazovksii model from five ($\tilde{\lambda}$, $\tilde{\gamma}$, $\tilde{\tau}$, $\tilde{\xi}$, and q_0) to two (τ and γ, defined below):

$$\begin{aligned}
\mathbf{r} &= q_0\tilde{\mathbf{r}}, \\
\phi\left(\mathbf{r}\right) &= \left[2\sqrt{\tilde{\lambda}}/\left(q_0\tilde{\xi}\right)\right]\tilde{\phi}\left(\mathbf{r}/q_0\right), \\
F &= {q_0}^3 16\tilde{F}\tilde{\lambda}/\left(q_0\tilde{\xi}\right)^4, \\
\tau &= 4\tilde{\tau}/\left(q_0\tilde{\xi}\right)^2, \\
\gamma &= 2\tilde{\gamma}/\left(q_0\tilde{\xi}\sqrt{\tilde{\lambda}}\right).
\end{aligned} \tag{1.2}$$

It is our understanding that this reduction of the effective number of parameters in this model (that is, the number of parameters defining the phase behavior of the model) from five to two has never before been discovered for this model, although others have reduced the parameter count in this model to three [36, 41]. Also, instead of the free energy F, we will consider the free energy density $f = F/V$, where V is the volume of the system with respect to the re-scaled length scale. This allows us to compare the free energies of periodic ordered structures by comparing the free energy *densities* of unit cells of those structures. Hence, Eqs. (1.1) and (1.2) yield:

$$f = \frac{1}{V}\int_{\Delta} \mathrm{d}^3\mathbf{r}\left[\frac{1}{2}\left(\nabla^2\phi + \phi\right)^2 + \frac{\tau}{2}\phi^2 - \frac{\gamma}{3!}\phi^3 + \frac{1}{4!}\phi^4\right], \tag{1.3}$$

where Δ is the domain of integration in $\mathbf{r}$-space. The order parameter field ϕ represents the thermal average of some physical quantity, and is exactly zero ($\phi(\mathbf{r}) = 0 \forall \mathbf{r}$) in the disordered phase. ϕ typically satisfies Eq. (1.4) below [36]. This is the case, for instance, if ϕ represents the deviation of mass or number density from its average, for then Eq. (1.4) is implied by mass conservation.

$$\int_{\Delta} \phi(\mathbf{r})\, \mathrm{d}^3\mathbf{r} = 0. \tag{1.4}$$

τ in Eq. (1.3) is a temperature-like parameter which, when negative, tends to induce stronger average segregation as it increases in magnitude.[5] τ also controls the onset of the order-disorder spinodal: the disordered phase becomes unstable at $\tau = 0$.

Our model exhibits a first-order phase transition for some $\tau > 0$ provided $\gamma \neq 0$. If $\gamma = 0$, the model has a second-order phase transition at the critical point ($\gamma = 0, \tau = 0$). For any given system, the Landau-Brazovskii model can only be expected to be strictly valid near the critical point. This is a result

---

[5] Since τ multiplies ϕ^2, if $\tau < 0$, the τ term is more negative when there is greater root-mean-square deviation from the spatial average of the order parameter, 0.

of the first-order nature of the transition: in general the order parameter field changes discontinuously across the order-disorder transition. Hence, the order parameter field cannot be expected in general to be small, even near the order-disorder transition. One can expect the order parameter field to be small near the critical point, since the order-disorder transition is continuous at the critical point. When we analyze the phase diagram of the Landau-Brazovskii model, we will be looking at regions where γ is large ($\gamma \sim 1$), far away from the critical point. We cannot expect the Taylor expansion in Eq. (1.3) to hold in such regions. However, one still may expect this functional to be qualitatively useful, even far from the critical point. One could, for instance, fit the phenomenological parameters in the Landau-Brazovskii model to experimental data, or to data generated by a superior model. In what follows, we treat the Landau-Brazovskii model as a general phenomenological model for the description of order-disorder phase transitions in which a periodic phase emerges with a single dominant wavelength.

1.3.1 Phase Diagram

The primary purpose of this work is to construct a phase diagram for the Landau-Brazovskii model. The stable phase of Eq. (1.3) at any given γ and τ is that minimizing the free energy density f. It is not feasible to directly compute the *global* minimum of f; however, with suitable numeric optimization techniques one can compare the optimal free energies for a number of candidate structures, selecting as the stable phase the phase with the lowest free energy. This was done, for instance, by Shi in [36], where the free energies for the disordered phase, cylindrical hexagonal phase, lamellar phase, BCC phase, and double gyroid phase (space group: $Ia\overline{3}d$) were compared to produce a phase diagram in the γ-τ plane. Shi found regions of stability for all of the phases mentioned above [36]. His diagram was later qualitatively reproduced by [41], and we also qualitatively reproduced his diagram by considering the same candidate phases (see Fig. 1.4). This "candidate phase approach" does not, of course, exclude the possibility that other phases, not in the list of candidate phases, are stable in some regions of the phase diagram. Nevertheless, this approach allows us to identify the relative stability among the phases considered. I will shortly present the phase diagram we constructed for the Landau-Brazovskii model; first, however, I discuss in the following chapter how we produced this diagram.

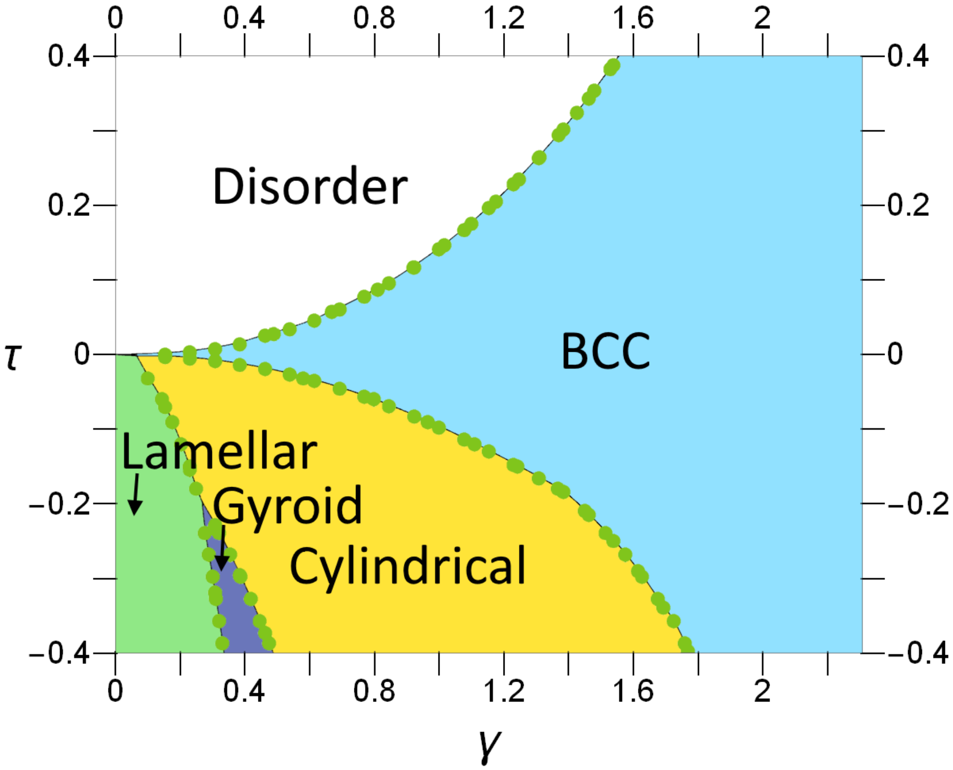

Figure 1.4: Original Landau-Brazovskii model phase diagram, similar to that obtained by previous researchers [36, 41]. Phase boundary points are shown with green dots; the lines connecting the points are cubic interpolations that were added as a guide to the eyes. This diagram was produced using the method described in Chap. 2.

Chapter 2

Methods

The primary goal of this work is to construct a phase diagram for the Landau-Brazovskii free energy functional defined by Eq. (1.3). This diagram, presented in Fig. 3.1, was produced by comparing the free energy densities of a number of candidate structures, including the σ and A15 Frank-Kasper phases. The candidate phases included all the phases that were found in the phase diagrams of [36] and [41] (the disordered, lamellar, BCC, cylindrical hexagonal, and double gyroid phases), as well as the face-centered-cubic (FCC) phase, and the aforementioned Frank-Kasper A15 and σ phases. We here present in detail our numerical method for constructing our phase diagrams.

2.1 Rescaling of Landau-Brazovskii Model

When creating the phase diagram for the Landau-Brazovskii model, we did not actually work with the functional in Eq. (1.3), but with the different rescaling of Eq. (1.1) given below [36, 41]:

$$f' = \frac{1}{V}\int_{\Delta} \mathrm{d}^3\mathbf{r}\left[\frac{(\xi')^2}{2}\left(\nabla^2\psi + \psi\right)^2 + \frac{\tau'}{2}\psi^2 - \frac{\gamma'}{3!}\psi^3 + \frac{1}{4!}\psi^4\right]. \tag{2.1}$$

The parameters in this equation are related to those in Eq. (1.3) as follows, as can be easily verified:

$$\begin{aligned} f' &= (\xi')^4 f, \\ \psi &= \xi'\phi, \\ \tau' &= (\xi')^2\tau, \\ \gamma' &= \xi'\gamma. \end{aligned} \tag{2.2}$$

The phase diagram of Eq. (2.1) is identical to that associated with Eq. (1.3), as long as the relationships of τ', γ', and ξ' with τ and γ are taken into account. Initially, I computed the phase diagram of Eq. (2.1) for several different values of ξ', but all appeared to produce nearly the same diagram when these relationships were considered, as expected. The phase diagram presented in this thesis (Fig. 3.1) was produced by finding a phase diagram for Eq. (2.1) by setting $\xi' = 0.65$, and then using Eq. (2.2) to relate τ' and γ' to the parameters τ and γ appearing in Eq. (1.3) and Fig. 3.1.

2.2 Construction of Phase Diagrams

The equilibrium phase of Eq. (2.1) for any given ξ', γ', and τ' is that with the lowest free energy density (henceforth, I shall use the terms "free energy density" and "free energy" interchangeably). Therefore, to produce a phase diagram for Eq. (2.1), we numerically located the minimal free energies of several different ordered phases at various values of γ' and τ', and then interpolated this free energy data to find the phase boundaries. In this section, I will discuss this procedure in more detail.

First, let us note that the order parameter field ψ appearing in Eq. (2.1) is subject to the following constraint (from Eq. (1.4) and Eq. (2.2)):

$$\int_{\Delta} \psi \, \mathrm{d}^3\mathbf{r} = 0. \tag{2.3}$$

Also, let us define T to be the set consisting of the ordered pairs (γ', τ') where γ' ranges from 0 to 1.5 in increments of 0.05, and τ' ranges from -0.2 to 0.2 in increments of 0.0125. T defines the set of parameter values at which free energies of the different phases were numerically estimated (ξ' is fixed at 0.65).

Below, I describe the procedure by which these free energy values can be obtained, and how they can be used to produce a phase diagram for the Landau-Brazovskii model.

1. For each pair (γ', τ') in T, assign free energies to the phases considered in our study, that is, to the disordered, lamellar, double gyroid, cylindrical hexagonal, BCC, FCC, σ, and A15 phases. Let us use the notation (P, a) to denote the combination of a given phase P and a given element $a \in T$ (the free energy of (P, a) is the free energy of phase P for the τ' and γ' values corresponding to a). The free energy assigned to (P, a) is determined as follows:

   (a) If P is the disordered phase, assign (P, a) the free energy zero.
   (b) Otherwise, choose an initial density profile (i.e., an initial order parameter field $\psi(\mathbf{r})$) which approximates the structure of phase P, and choose the initial width, length, and height of the simulation box. This step is discussed in detail in §2.3.
   (c) To ensure a fair comparison between the free energies of the different ordered phases, we must determine the optimal (minimum) free energy for each phase, and then compare these optimal free energies to determine the equilibrium phase. Hence, numerically minimize the free energy f' subject to Eq. (2.3), with the initial condition mentioned above. Our goal is to find a local minimum of f' whose basin of attraction includes the aforementioned initial condition. Assign the resulting, minimized, free energy density to (P, a). If the minimization algorithm fails to converge, note that an error occurred and record the error. This step is discussed in detail in §2.4.

2. Next, create the phase diagram using the free energies found for all the pairs (P, a). This step is discussed in more detail in §2.5.

3. Finally, perform verification procedures to ensure the ordered phases found in the phase diagram actually are the structures they claim to be. Although we choose (when running our minimization algorithm for a given phase) an initial condition corresponding to the phase of interest, it is possible that our minimization algorithm might cause this phase to decay to a different ordered phase. This verification procedure is described in Appendix D.

We now consider three of the steps mentioned above in greater detail.

2.3 Choice of Initial Conditions for each Phase

After selecting a particular phase P, we must choose the initial order parameter field we wish to use when minimizing the free energy f' for given τ' and γ' values. Table 2.1 gives the expressions used to generate the initial density profile for each ordered phase. This table also includes the initial lattice parameters and dimensions (width $= W$, length $= L$, and height $= H$) of the simulation box used with a given phase. In Table 2.1, we split the position vector $\mathbf{r}$ into its components along the x, y, and z directions, so that $\mathbf{r} = x\hat{\mathbf{x}} + y\hat{\mathbf{y}} + z\hat{\mathbf{z}}$, where $\hat{\mathbf{x}}$, $\hat{\mathbf{y}}$ and $\hat{\mathbf{z}}$ form a right-handed triple, and are aligned with the axes of the simulation box (which is a right rectangular prism). For any given phase, the origin $\mathbf{r} = \mathbf{0}$ sits at one corner of the simulation box.

Table 2.1: Initial density profiles and associated parameters, including the mathematical expressions ψ representing these structures. For the cubic and tetragonal unit cells in this table, a and c represent lattice parameters for the conventional unit cell, a being the length of that cell in the x and y directions, and c being its length in the z-direction (for cubic unit cells, of course, only a is needed). The symbols Λ_{A15}, Λ_{σ}, x_2, x_3, y_3, x_4, y_4, x_5, and z_5 are defined in the text following the table. Note: "HEX," "GYR", and "LAM" refer to "cylindrical hexagonal," "gyroid," and "lamellar," respectively.

Phase	**Expression ($\psi(\mathbf{r})$)**	**Parameter Values**
A15	$\left\{\begin{array}{ll} A\mathrm{e}^{-\frac{1}{1-d^2 {a_0}^{-2}}} - A' & \text{if } \Phi(\mathbf{r}), \\ -A' & \text{otherwise.} \end{array}\right\}$ with: $\Phi(\mathbf{r}) := (\exists \mathbf{r}' \in \Lambda_{A15}(a) \mid$ $d = \lvert\mathbf{r} - \mathbf{r}'\rvert \leq a_0)$	$a = L = W = H = 2\pi\sqrt{5}$, $a_0 = a/5.5$, $A = 3\mathrm{e}$
BCC	$A(\cos\dfrac{2\pi x}{a}\cos\dfrac{2\pi y}{a} +$ $\cos\dfrac{2\pi y}{a}\cos\dfrac{2\pi z}{a} +$ $\cos\dfrac{2\pi z}{a}\cos\dfrac{2\pi x}{a})$	$a = L = W = H = 2\pi\sqrt{2}$, $A = 1$
HEX	$A(\cos\frac{4\pi y}{\sqrt{3}a} + 2\cos\frac{2\pi x}{a}\cos\frac{2\pi y}{\sqrt{3}a})$	$a = 4\pi/\sqrt{3}$, $W = a$, $L = \sqrt{3}a$, $A = 1$
FCC	$A\cos\frac{2\pi x}{a}\cos\frac{2\pi y}{a}\cos\frac{2\pi z}{a}$	$a = L = W = H = 2\pi\sqrt{3}$, $A = 3$

Table 2.1: Initial density profiles and associated parameters *cont.*

Phase	**Expression**	**Parameter Values**
GYR	$\begin{Bmatrix} -A' & \text{for } f(\mathbf{r}) \in [-\alpha, \alpha], \\ A - A' & \text{otherwise.} \end{Bmatrix}$ with: $f(\mathbf{r}) := \sin\frac{2\pi y}{a}\cos\frac{2\pi z}{a} + \sin\frac{2\pi z}{a}\cos\frac{2\pi x}{a} + \sin\frac{2\pi x}{a}\cos\frac{2\pi y}{a}$	$a = L = W = H = 2\pi\sqrt{6}$, $A = 3$, $\alpha = 1$
LAM	$\cos\frac{2\pi x}{L}$	$L = 2\pi$
σ	$\begin{Bmatrix} Ae^{-\frac{1}{1-d^2 {a_0}^{-2}}} - A', & \text{if } \Phi(\mathbf{r}) \\ -A', & \text{otherwise} \end{Bmatrix}$ with: $\Phi(\mathbf{r}) := (\exists \mathbf{r}' \in \Lambda_\sigma(a, c, x_2, x_3, y_3, x_4, y_4, x_5, z_5) \mid d = \lvert \mathbf{r} - \mathbf{r}' \rvert \leq a_0)$	$a = (2\pi)4.44$, $c = (2\pi)2.27$, $L = W = a$, $H = c$, $A = 3\text{e}$, $a_0 = c/6$, $x_2 = 0.39$, $x_3 = 0.46$, $y_3 = 0.13$, $x_4 = 0.74$, $y_4 = 0.07$, $x_5 = 0.18$, $z_5 = 0.25$

Fig. 2.1 gives isosurface plots of the initial density profiles for the different candidate structures. A few remarks about Table 2.1 are in order. a, in the case of the cylindrical hexagonal phase, refers to the smallest distance between lattice sites in the hexagonal lattice. The symbol A' is a constant that is always defined so that Eq. (2.3) is met for the initial density profile.

The initial conditions for the BCC, cylindrical hexagonal, FCC, and lamellar phases are single-wavenumber approximations of Fourier expansions associated with these structures. The gyroid phase initial condition is obtained by assigning the positive constant $A - A'$ to any point in a union of regions bounded by the two level surfaces $\sin\frac{2\pi y}{a}\cos\frac{2\pi z}{a} + \sin\frac{2\pi z}{a}\cos\frac{2\pi x}{a} + \sin\frac{2\pi x}{a}\cos\frac{2\pi y}{a} = \pm\alpha$ (see, e.g., [42] or [43]) and assigning the constant $-A'$ to any point not in this union of regions. Turning to our choice of initial lattice parameters for the different ordered phases, I note first that the initial period chosen for the lamellar phase (2π) is a natural choice designed to minimize the $\left(\nabla^2\psi + \psi\right)^2$ term in the free energy (Eq. 2.1). The lattice parameters for the BCC, cylindrical hexagonal, FCC, double gyroid, and lamellar phases come from epitaxial relationships between these phases. In particular, we used the cylindrical-lamellar epitaxial relationship given in [44], the cylindrical-BCC relationship given for a block copolymer melt in [45], the BCC-FCC relationship given for a block copolymer solution in [46], and the lamellar-gyroid or cylindrical-gyroid relationship found for a lyotropic liquid crystalline system in [47] (which is also found in other systems; see [48] for a review).

The initial conditions for the A15 and σ phases are generated as follows. First, our algorithm defines the simulation box as the conventional unit cell for the phase of interest. a_0 is defined to be the radius of the "atoms" (regions where $\psi > -A'$) in the structure. The sets Λ_{A15} and Λ_σ each refer to the set of atomic positions which are either within the simulation box, or within a distance a_0 from an edge of the simulation box. For a point $\mathbf{r}$ in the unit cell that is within one of the atoms, so that the condition $\Phi(\mathbf{r})$ (see Table 2.1) holds, the distance d to the center of the atom is computed by our algorithm. When d is determined, the value of the initial density profile at $\mathbf{r}$ is given by a "bump function" (see Table 2.1) which reaches its maximum value of $A - A'$

at the center of the atom, and goes smoothly to $-A'$ as $d \to a_0$. If our point with position $\mathbf{r}$ is not inside an atom, the density profile at that point is simply assigned a constant value of $-A'$. In this way, we create a smooth initial density profile which takes on higher values in the vicinity of an "atom" associated with the structure of interest.

Note that the quantities x_2, x_3, y_3, x_4, y_4, x_5, and z_5 in Table 2.1 are adjustable parameters that define the precise way in which the atoms in the σ phase are configured (see §A.2). Our choice for these parameters comes from [49].

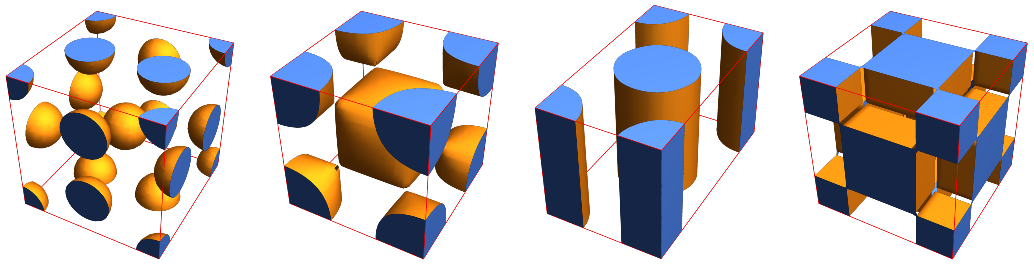

(a) A15 (b) BCC (c) Hexagonal (d) FCC

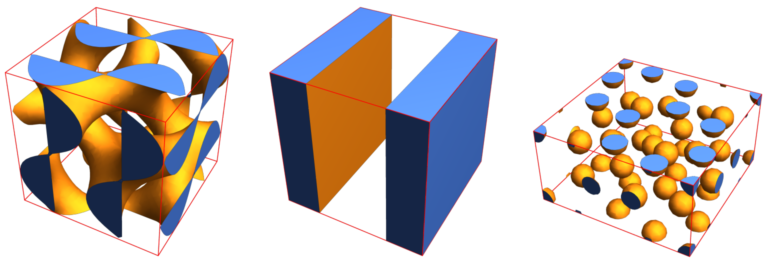

(e) Double gyroid (f) Lamellar (g) σ

Figure 2.1: Plots of initial density profiles. The filled yellow regions represent the minority domains, where the order parameter field is positive. Note that the lamellar and cylindrical hexagonal phases are shown in three dimensions for ease of viewing, but were treated as one- and two-dimensional phases, respectively, by our minimization program.

We now consider the initial lattice parameter (a) for the A15 phase. The ratio between this value and our initial BCC a-value closely matches that found experimentally in certain ionic surfactant systems [6] and in numerical diblock copolymer SCFT calculations [29].

The ratio c_σ/a_{BCC}, between our initial c parameter for the σ phase and our initial a parameter for the BCC phase, is close to that found in certain simulations and experiments of diblock copolymer melts [29] and in certain ionic surfactant systems [6]. Likewise, the ratio c/a for the initial σ phase condition is close to (within 5% of) the value found experimentally in certain diblock copolymer [11, 29], ionic surfactant [6], and giant surfactant [50] systems.

2.4 Minimization Procedure

Next, we consider the process of finding a local minimum of f' (Eq. (2.1)), given ξ', γ', τ', and a phase P with its associated initial density profile ψ_0. We impose periodic boundary conditions. Furthermore, we assume that the simulation box with domain Δ is three-dimensional, but the procedure herein can easily be modified for the two- and one-dimensional cases. We also impose the constraint given by Eq. (2.3). If P is metastable or stable at our values of ξ', γ', and τ', then we expect that locally minimzing f' will produce the optimal free energy of phase P for these parameter values, because the initial condition used when we perform the local minimization approximates the structure of phase P. If P is unstable for these parameter values, the minimization algorithm will cause the initial density profile ψ_0 associated with P to change to some other structure. In this case, the final minimized free energy produced by the minimization algorithm will not be that of P, but of some other structure. We explain how we deal with this in §2.5 and Appendix D. For now, we simply explain how we numerically minimize Eq. (2.1) subject to some initial density profile (associated with a phase P) and with certain parameter values ξ', γ', and τ'.

2.4.1 Minimization Problem Formulation

Minimizing f' involves the determination of the optimal density profile $\psi_f(\mathbf{r})$ and the optimal simulation box dimensions. Focusing on the determination of the density profile, we will consider the problem in which the simulation box dimensions are fixed, and will return later to the problem of determining optimal values for these dimensions. We must minimize Eq. (2.1) subject to Eq. (2.3) over the space of density profiles $\psi(\mathbf{r})$. The constraint makes the optimization problem significantly more complicated. There are a number of ways to deal with it. We chose to reformulate the minimization problem as an ordinary differential equation whose independent variable is a pseudo-time parameter t, such that as $t \to \infty$, the order parameter field approaches the order parameter field with the locally minimal value of f'.

Roughly, we may derive the differential equation we used in the following way. We can define a space-dependent chemical potential $\mu(\mathbf{r})$ by taking the variational derivative of f' with respect to the order parameter field ψ:

$$\mu := \frac{\delta f'}{\delta \psi}.$$

Since we are seeking the minimal value of f' under the constraint in Eq. (2.3), we will formulate our pseudotime evolution such that the free energy f' decreases with t. We also will ensure that the constraint in Eq. (2.3) is satisfied for all t. To do so, we design a pseudotime evolution equation that locally conserves ψ, and follows the negative gradient of the chemical potential. This latter consideration guarantees that f' is nonincreasing with t, and the local conservation ensures that the constraint given by Eq. (2.3) is always satisfied, provided it is satisfied by the initial density profile. In other words, we allow ψ to pseudotime-evolve under a current density $\mathbf{J}$ given by:

$$\mathbf{J} = -\eta \nabla \mu,$$

where $\eta > 0$ is a constant. Since our order parameter is locally conserved, it must change with t according to the continuity equation:

$$\frac{\partial \psi}{\partial t} = -\nabla \cdot \mathbf{J}.$$

Combining the three equations above yields:

$$\frac{\partial \psi}{\partial t} = \eta \nabla^2 \left[\frac{\delta f'}{\delta \psi} \right]. \tag{2.4}$$

Because of the definition of $\mathbf{J}$, Eq. (2.4) ensures that f' will be nondecreasing with time (provided that ψ satisfies periodic boundary conditions). Furthermore, the “maximum principle” for harmonic functions ensures that the steady state ($\frac{\partial \psi_f}{\partial t} = 0$) solutions ψ_f to Eq. (2.4) will be uniformly constant (again, given periodic boundary conditions), i.e.,

$$\psi_f\left(\mathbf{r}\right) = K,$$

for some K. If we interpret K as a Lagrange multiplier associated with the constraint given by Eq. (2.3), we see that the steady state solutions to Eq. (2.4) satisfy the first-order optimality conditions for f' subject to Eq. (2.3), provided the initial density profile satisfies Eq. (2.3). However, ψ_f need not be a local minimum – it could be the constrained optimization analogue of a saddle point. We assume that our initial density profiles are close enough to their optimized counterparts that such behavior does not occur.

To solve Eq. (2.4) given some initial order parameter field ψ_0, we cannot simply apply standard explicit methods, as the equation is too unstable. The explicit Euler and Runge-Kutta methods, for instance, demand impractically small time steps. We also cannot easily apply standard implicit methods, because of the nonlinear nature of Eq. (2.1). Fortunately, more suitable algorithms exist. I created a C++ implementation of the first-order "scalar auxilary variable" algorithm [51, 52], which enabled us to efficiently find steady state solutions of Eq. (2.4).

2.4.2 Density Profile Real-Space Discretization

In order to solve Eq. (2.4), we must find some method of representing the density profile ψ – a function of a continuous variable $\mathbf{r}$ – in finite computer memory. To do so, we divide the simulation box Δ into a grid of discrete points. Let there be N points along the x-direction, M along the y-direction, and L along the z-direction. The position $\mathbf{r}_{ijk}$ of any point in the grid is given by $\mathbf{r}_{ijk} = (\Delta W)\, i\hat{\mathbf{x}} + (\Delta L)\, j\hat{\mathbf{y}} + (\Delta H)\, k\hat{\mathbf{z}}$, where ΔW, ΔL, and ΔH represent the spacings between grid points in the x, y, and z directions, respectively. i, j, and k range between 0 and $N-1$, $M-1$, and $L-1$, respectively. We can thus represent ψ approximately by the set of values of ψ at all the points in the aforementioned grid. This set we indicate with $\{\psi(\mathbf{r}_{ijk})\}$.

2.4.3 Density Profile Fourier-Space Discretization

Now, since $\psi(\mathbf{r})$ is a periodic function, we may represent it as a multidimensional Fourier series. Let $\mathcal{F}_{\mathbf{q}}[\psi]$ be the operator yielding the Fourier component $\hat{\psi}(\mathbf{q})$ of ψ corresponding to wavevector $\mathbf{q}$. $\mathcal{F}_{\mathbf{q}}$ satisfies the following well-known relation:

$$\mathcal{F}_{\mathbf{q}}\left[\nabla^2\psi\right] = -q^2\mathcal{F}_{\mathbf{q}}[\psi]\,. \tag{2.5}$$

If we assume that ψ changes sufficiently slowly over real space, we expect that the high-frequency (high-q) Fourier components will be very small, and that we can approximate ψ with a partial Fourier series consisting only of the low-q Fourier terms.

This is the motivation underlying the discrete Fourier transform (DFT). The DFT of the discretized real-space ψ-data $\{\psi(\mathbf{r}_{ijk})\}$ consists of a set of estimates for the Fourier components at specific locations on a grid in Fourier space. In particular, the DFT of $\{\psi(\mathbf{r}_{ijk})\}$ can be written as $\left\{\hat{\psi}\left(\mathbf{q}_{\hat{i}\hat{j}\hat{k}}\right)\right\}$, where:

$$\hat{\psi}\left(\mathbf{q}_{\hat{i}\hat{j}\hat{k}}\right) = \sum_{k=0}^{L-1}\sum_{j=0}^{M-1}\sum_{i=0}^{N-1} \psi\left(\mathbf{r}_{ijk}\right) \mathrm{e}^{-i\mathbf{q}_{\hat{i}\hat{j}\hat{k}}\cdot\mathbf{r}_{ijk}}, \tag{2.6}$$

with $\mathbf{q}_{\hat{i}\hat{j}\hat{k}} = \left(2\pi\hat{i}/W\right)\hat{\mathbf{x}} + \left(2\pi\hat{j}/L\right)\hat{\mathbf{y}} + \left(2\pi\hat{k}/H\right)\hat{\mathbf{z}}$. $\hat{i}$, $\hat{j}$, and $\hat{k}$ index a grid point in $\mathbf{q}$-space, with $-\lceil\frac{N}{2}\rceil + 1 \leq \hat{i} \leq \lfloor\frac{N}{2}\rfloor$, $-\lceil\frac{M}{2}\rceil + 1 \leq \hat{j} \leq \lfloor\frac{M}{2}\rfloor$, and $-\lceil\frac{L}{2}\rceil + 1 \leq \hat{k} \leq \lfloor\frac{L}{2}\rfloor$. We can also invert the DFT $\left\{\hat{\psi}\left(\mathbf{q}_{\hat{i}\hat{j}\hat{k}}\right)\right\}$ to obtain the original real-space discretization of ψ:

$$\psi\left(\mathbf{r}_{ijk}\right) = \frac{1}{MNL}\sum_{\hat{k}=-\lceil\frac{L}{2}\rceil+1}^{\lfloor\frac{L}{2}\rfloor}\;\sum_{\hat{j}=-\lceil\frac{M}{2}\rceil+1}^{\lfloor\frac{M}{2}\rfloor}\;\sum_{\hat{i}=-\lceil\frac{N}{2}\rceil+1}^{\lfloor\frac{N}{2}\rfloor} \hat{\psi}\left(\mathbf{q}_{\hat{i}\hat{j}\hat{k}}\right) \mathrm{e}^{i\mathbf{q}_{\hat{i}\hat{j}\hat{k}}\cdot\mathbf{r}_{ijk}}, \tag{2.7}$$

Assuming that the DFT of $\{\psi\left(\mathbf{r}_{ijk}\right)\}$ contains enough Fourier components to approximate ψ sufficiently well, we can simplify certain calculations. For instance, if we want to estimate the Laplacian $\nabla^2\psi$ of ψ given discretized real-space data $\{\psi\left(\mathbf{r}_{ijk}\right)\}$, we may do so by computing the DFT of this real-space data, applying Eq. (2.5) to the Fourier components generated by the DFT, and then (if we wish) changing back to a real space representation with Eq. (2.7). This fact will be useful when we study the algorithm we use to minimize the free energy f'.

2.4.4 Overview of Minimization Algorithm

Let us now return to the problem of minimizing f' given some phase P and particular values for ξ', γ', and τ'. To perform this minimization, we used the procedure below:

1. Define a simulation box whose initial size is given by Table 2.1. Then, compute the real-space discretization $\{\psi(\mathbf{r}_{ijk})\}$ of the initial density profile associated with the phase of interest. If P is the σ phase, let this discretization consist of 128 points along the x- and y-directions, and 64 points along the z-direction; in other words, use a $128 \times 128 \times 64$ discretization. If P is the cylindrical hexagonal phase, use a $64 \times 128 \times 1$ discretization. If P is the lamellar phase, use a $64 \times 1 \times 1$ discretization. If P is any other phase, use a $64 \times 64 \times 64$ discretization.

2. Fixing the size of the simulation box, use our implementation of the first order scalar auxiliary variable (SAV) method (see Appendix B) to locate the local minimum of f'. Use a maximum iteration count of 100,000 and a relative tolerance of 10^{-13}. If the maximum iteration count is reached during execution of the SAV algorithm, abort the minimization process.

3. Using the discrete Fourier transform (DFT) of the final density profile data produced in the previous step, minimize the free energy density f' with respect to the width, length, and height of the simulation box. When performing this minimization, we fix the discretized field values $\{\psi(\mathbf{r}_{ijk})\}$: we only stretch the density profile affinely along the principle axes of the simulation box. See Appendix C for details.

4. Repeat the two steps above until the relative difference between the free energies before and after the period optimization reaches 10^{-13}. Call the discretization of the final, minimized density profile $\{\psi_f(\mathbf{r}_{ijk})\}$.

5. Double the number of points, in each direction, of the real space discretization grid constructed in step one (except for the lamellar phase, in which the number of points is only doubled along the x-direction, and

for the cylindrical hexagonal phase, in which the number of points is doubled only along the x and y directions, because these are one- and two-dimensional phases, respectively).

6. Using the lower-resolution discretization $\{\psi_f(\mathbf{r}_{ijk})\}$ of the final, minimized field produced in step four, generate a high resolution version of this final condition on the new higher resolution grid, and use this as the initial condition to repeat steps 2-4. Declare the resulting free energy the free energy of the structure in question at the values of ξ', γ', and τ' we are considering.

2.5 Production of Phase Diagram from Minimized Free Energy Data

Once the minimized free energy data is collected for each phase and set of parameters $a \in T$, it remains to produce a phase diagram. This was effectively done in three stages, which are given below.

1. First, create a preliminary phase diagram, showing the "equilibrium" phase (i.e., the lowest free energy phase among those considered) at each point $a \in T$. In this way, the general topology of the phase diagram can be ascertained. Make note of any small, anomalous groupings of points $a \in T$ in which the indicated stable phase is different than that for a larger region of points in which these points lie. The phase (that is, the lowest free energy phase) associated with these isolated groupings is probably unstable at these points, and the minimization algorithm has

probably caused this phase to decay to the phase associated with the larger, surrounding region in which these isolated points sit. Verify this by examining $\psi_f = 0$ isosurface plots (here ψ_f for a given a represents the final, optimized density profile at point a and associated with the phase which has the lowest free energy at a) for all the points in T in these anomalous groupings – these plots should show a structure matching the equilibrium structure for the surrounding region in which these points sit.[1] Change the assigned phase of any such anomalous points (at which the equilibrium phase is falsely identified) to the correct phase.

2. We will soon attempt to use quadratic interpolation to estimate the location of the phase boundaries. First, however, I note that, at some points $a \in T$ – especially close to the order-disorder line of stability – our algorithm failed to converge, or caused some ordered phases to decay to the disordered phase when these phases should be metastable. One can attempt to identify these problematic points in the following way. First, apply the following procedure to each point $a \in T$:
    (a) Determine the equilibrium phase associated with a. Call this phase P. If P is the disordered phase, skip the following steps.
    (b) Then, apply the step below to each nearest neighbour a' to a.
    (c) Sometimes, the free energy of P at a' is very close to the disordered phase free energy (we identified a free energy as the disordered free energy if it was within $[-10^{-10}, 10^{-8}]$), or our algorithm does not

---

[1] I did indeed have to do this for five points in the A15 region, and the actual lowest free energy phase at these points was indeed the A15 phase. Note that if we look at values of τ greater than those indicated in the diagram, there seems to be a location at which some other phase that I did not consider becomes stable, but I did not investigate this in detail.

converge at a' when considering phase P. Since it is unusual for a phase to jump from being stable at a to being unstable at a', given the first-order nature of all phase transitions[2] in the Landau-Brazovskii model, we would like to investigate this behavior to ensure that it is not a computational artifact. To do so, attempt to apply step three below to locate the phase boundary point between a and a'. If the phase boundary point cannot be found using that interpolation procedure, that is an indication that P may not actually be unstable at a'. To estimate the real free energy of P at a', use quadratic extrapolation from points near a' where P converges to determine a new free energy for P at a'.

Repeat the procedure above until all anomalies have been corrected.[3]

3. Using the new, updated free energies from the previous step, identify points on the boundaries between the different phase regions by performing quadratic interpolation of the free energies computed by our algorithm for each phase. I obtained these boundary points by fixing different values of τ' and looking for phase boundaries along the γ' direction, and by fixing different values of γ' and looking along the τ' direction. For instance: if one is moving along the τ' direction, let us say that steps one and two indicate that the cylindrical hexagonal phase is the stable phase at $(\gamma' = 0.3, \tau' = -0.05)$ and that the BCC phase is stable at the next point along the τ' direction, $(\gamma' = 0.3, \tau' = -0.0375)$.

---

[2] Except at the critical point.

[3] In my case, most anomalies were corrected after one iteration of the procedure above. However, there were some points close to the cylindrical-A15 phase boundary in the high-γ, low-τ region of the phase diagram which required multiple applications of the procedure above to correct all anomalies.

One could then obtain the phase boundary point at $\gamma' = 0.3$ and with $\tau' \in [-0.05, -0.0375]$ by performing quadratic interpolation of the *difference* between the free energy of the BCC phase and the free energy of the cylindrical phase, and finding the zero of this interpolating function.

4. Finally, we connected the phase diagram boundaries with smooth cubic interpolations to obtain the phase boundary curves visible in Fig. 3.1.

Chapter 3

Results

The phase diagram of the Landau-Brazovskii model (Eq. (1.3)) is given in Fig. 3.1. The Frank-Kasper σ and A15 phases are stabilized as γ is increased past around 0.8. Interestingly, the FCC phase is also stable in the upper-right region of the phase diagram. Such behavior has not previously been found; to my knowledge, neither the σ nor the A15 phase have hitherto been identified in the Landau-Brazovskii model. Indeed, up till now, no one has (to my knowledge) even considered these phases in the context of this model. The contrast between the behavior of the old Landau-Brazovskii phase diagrams and our new diagram can be seen in Fig. 3.2, where we have superimposed the phase boundary lines from Fig. 1.4 (the phase diagram without including the FCC, σ, or A15 phases as candidate structures) on the new phase diagram in Fig. 3.1. Fig. 3.2 shows that the spherical region of the new phase diagram roughly matches that of the old phase diagram, save that the σ and A15 phases cause the new spherical region to be slightly larger than the old.

The overall order-order phase transition sequence in Fig. 3.1 proceeds, as γ increases, from the lamellar phase, to the gyroid phase (a bicontinuous phase), to the cylindrical phase, and then to a spherical phase. As mentioned in §1.1, AB diblock copolymers exhibit a generic phase transition sequence from a lamellar to a cylindrical to a bicontinuous to a spherical phase, as the minority block fraction f_A is decreased from $f_A = \frac{1}{2}$. This phase transition sequence matches that found in the Landau-Brazovskii model: increasing the symmetry parameter γ corresponds to decreasing the minority block fraction f_A ($\gamma = 0$ would correspond to $f_A = \frac{1}{2}$ if the Landau-Brazovksii model were applied to a system of linear diblock copolymers in which each block had the same Kuhn length, as $\gamma = 0$ would correspond to the case of no asymmetry between the A and B blocks).

I also created plots from the final (optimized) density profile data produced using the algorithm in Chap. 2: either $\psi = 0$ isosurface plots (for the three-dimensional phases), "heat map" density plots (for the two-dimensional cylindrical hexagonal phase), or standard ψ *vs.* x plots (for the one-dimensional lamellar phase). These plots are shown in Fig. 3.3.

Additionally, I produced Fourier-space plots from the optimized density profile data used to generate the real-space plots in Fig. 3.3. Two of these plots, for the A15 and σ phases, are shown in Fig. 3.4, and the rest are found in Appendix E. On the x-axis, I plotted the Fourier-space wavevector magnitude q, and on the y-axis, the logarithm of a "scattering intensity." For a given q, this scattering intensity is simply (up to a constant) the average value of all of the square magnitudes of the discrete Fourier transform components corresponding to positions (in Fourier space) a distance q from the origin.

These plots should approximately match small-angle X-ray scattering (SAXS) plots obtained from real physical systems exhibiting the σ and A15 phases. Indeed, if we compare Fig. 3.4 with experimental SAXS plots [6] obtained from a small ionic surfactant system exhibiting the σ and A15 phases, we find remarkable agreement: the positions of the SAXS peaks for the A15 phase (Fig. 1 of [6]) are identical to the positions of the peaks in Fig. 3.4a, save for one extra peak in Fig. 3.4a with Miller indices (420). Likewise, the positions of the "main group" of SAXS peaks (starting at (310) and ending at (312)) for the σ phase (Fig. S1 in [6]) are identical to those in Fig. 3.4b, except for one extra peak at (420) in Fig. 3.4b. The relative magnitudes of the peaks are also qualitatively similar in both cases.

Finally, I include in this chapter two free energy density plots for different ordered phases. On the y-axes of these plots, I plot the excess free energy Δf, which is the difference between the minimized free energy density (f in Eq. (1.3)) of the phase of interest and the minimized free energy density of some reference phase. On the x-axes of these plots, I plot τ. The plotted points correspond to the free energy density values obtained with my minimization algorithm (after any anomalies have been corrected by step two of §2.5).

In Fig. 3.5a, for which $\gamma = 0.15$ and $\tau \in [-0.3, 0.1]$, one observes a phase transition from the lamellar to the cylindrical to the BCC to the disordered phase as τ increases. Note that the cylindrical phase is unstable for sufficiently negative values of τ (rather, it decays to the lamellar phase), but becomes metastable at $\tau \approx -0.25$. All phases in Fig. 3.5a decay to the disordered phase shortly after crossing the $\tau = 0$ point. In Fig. 3.5b, for which $\gamma = 1.23$ and $\tau \in [0.1, 0.36]$, one observes a phase transition sequence from the A15 to the σ to the FCC to the disordered phase as τ increases. As before, all phases decay to the disordered phase for sufficiently positive values of τ.

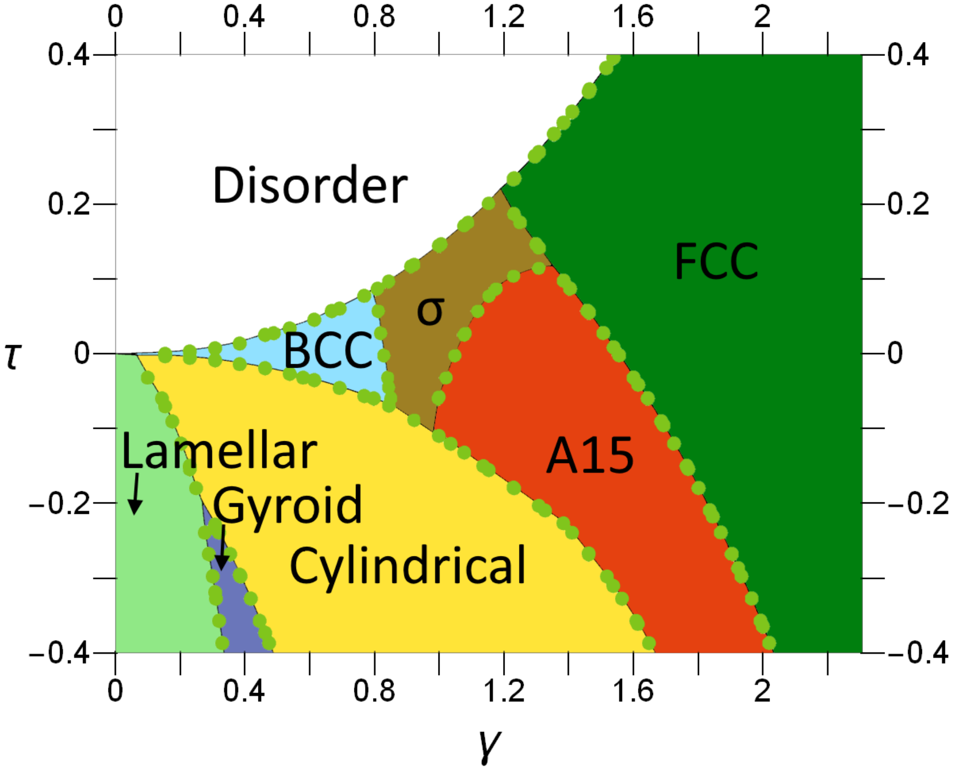

Figure 3.1: Landau-Brazovskii model phase diagram. Phase boundary points are shown with green dots; the lines connecting the points are cubic interpolations that were added as a guide to the eyes.

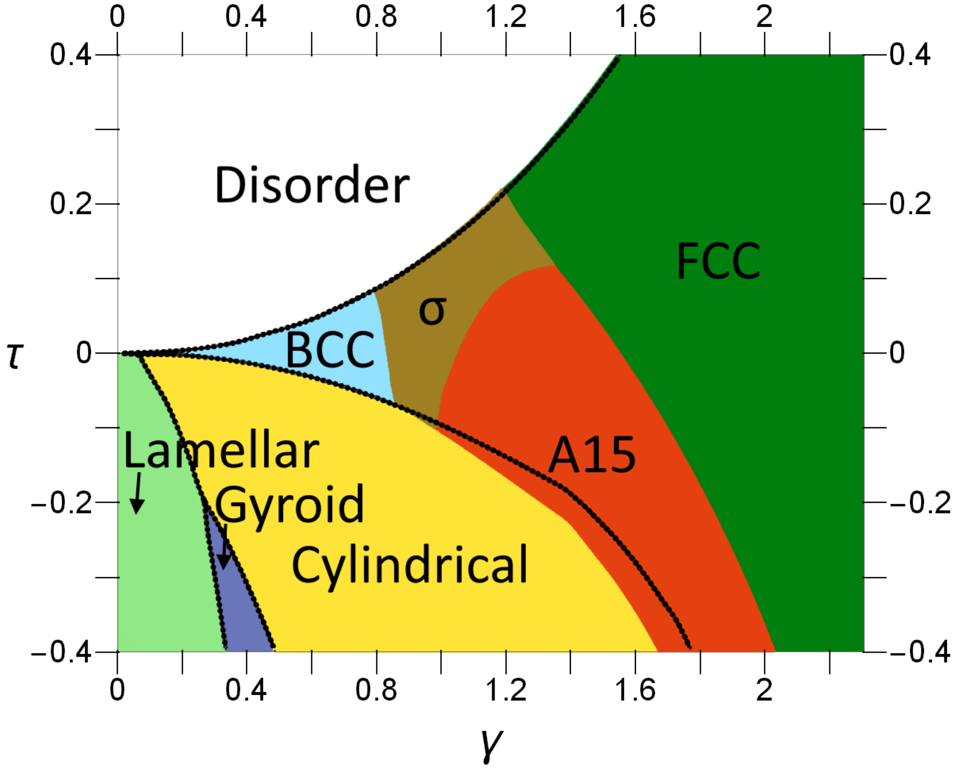

Figure 3.2: Landau-Brazovskii model phase diagram with phase boundaries from original phase diagram (without FCC, σ, or A15 phases) in Fig. 1.4. The phase boundaries from Fig. 1.4 are shown with dotted lines; the solid regions are those of the new phase diagram in Fig. 3.1.

Figure 3.3: Selected plots of final density profiles associated with the equilibrium phases in Fig. 3.1.

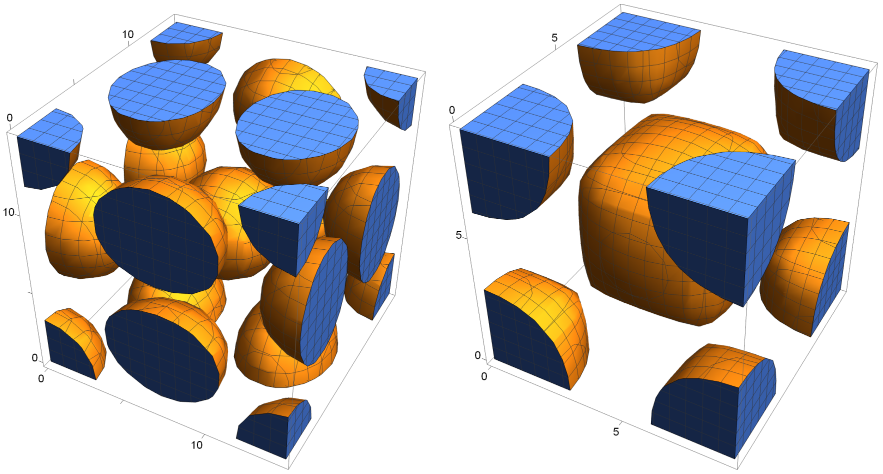

(a) A15 phase (at $(\gamma = 1.23, \tau = 0)$).

(b) BCC phase (at $(\gamma = 0.31, \tau = 0)$).

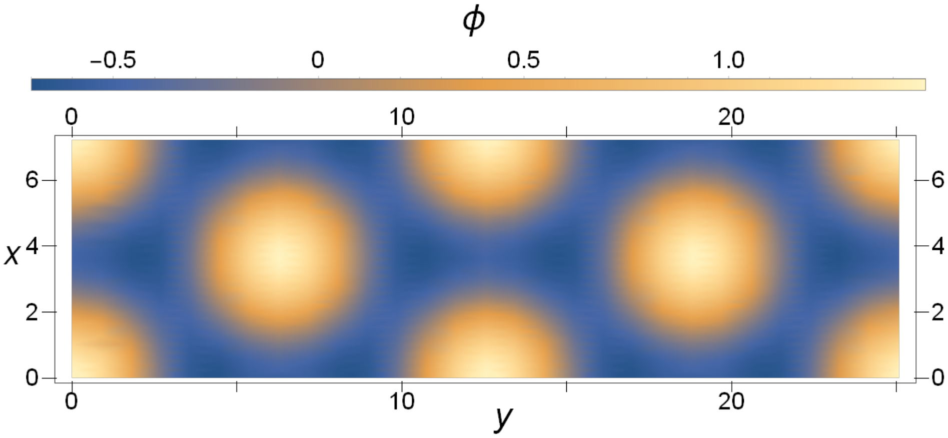

(c) Cylindrical hexagonal phase (at $(\gamma = 0.62, \tau = -0.12)$).

Figure 3.3: Selected plots of final density profiles *cont.*

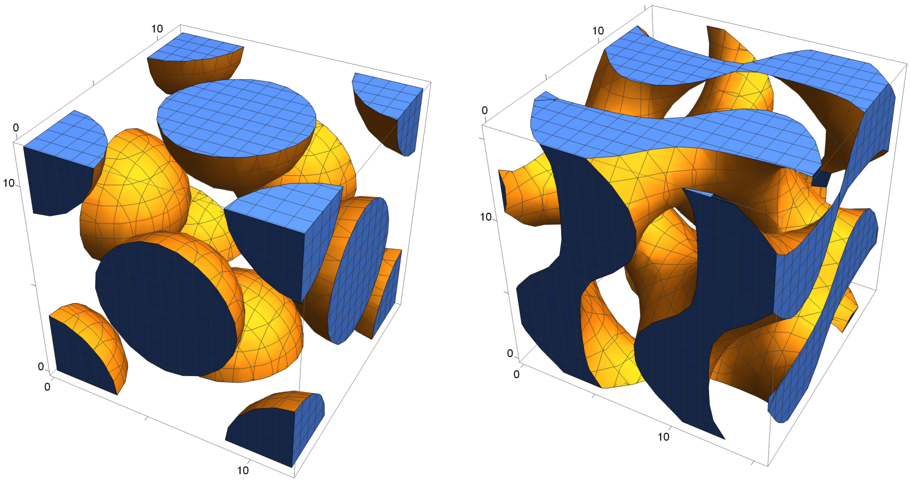

(d) FCC phase (at $(\gamma = 1.85, \tau = 0)$).

(e) Double gyroid phase (at $(\gamma = 0.46, \tau = -0.47)$).

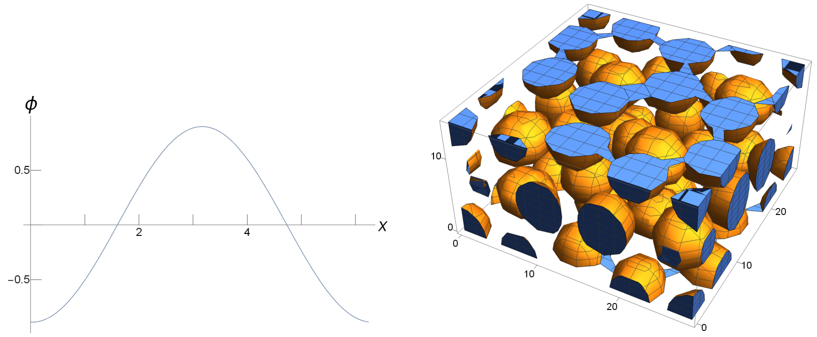

(f) Lamellar phase (at $(\gamma = 0.15, \tau = -0.24)$).

(g) σ phase (at $(\gamma = 1.08, \tau = -0.059)$).

Figure 3.4: Selected Fourier-space plots of final density profiles associated with two of the equilibrium phases, the σ and A15 phases, in Fig. 3.1. On the y-axis is plotted $\log\left[\frac{\left\langle|\hat{\psi}_{\mathbf{q}}|^2\right\rangle_{|\mathbf{q}|=q}}{\max_{\mathbf{q}}\left(\left\langle|\hat{\psi}_{\mathbf{q}}|^2\right\rangle_{|\mathbf{q}|=q}\right)}\right]$. In other words, the y-axis variable is the logarithm of a scaled average of the square magnitudes of the Fourier components (that is, the components of the discrete Fourier transform) $\hat{\psi}_{\mathbf{q}}$ of ψ, where the average for a given q is over all $\mathbf{q}$ with magnitude q, and q is plotted on the x-axis. If the argument to the logarithm above is less than 10^{-7}, the associated peak is omitted from its plot. The indices above each peak represent sample Miller indices corresponding to the peak in question (in rare cases two such sample Miller indices are included).

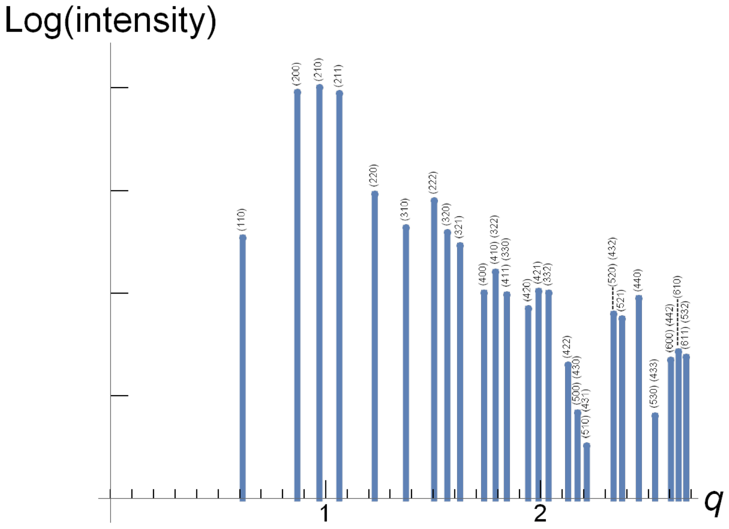

(a) A15 phase (at $(\gamma = 1.23, \tau = 0)$).

Figure 3.4: Selected A15 and σ Fourier-space plots of final density profiles *cont.*

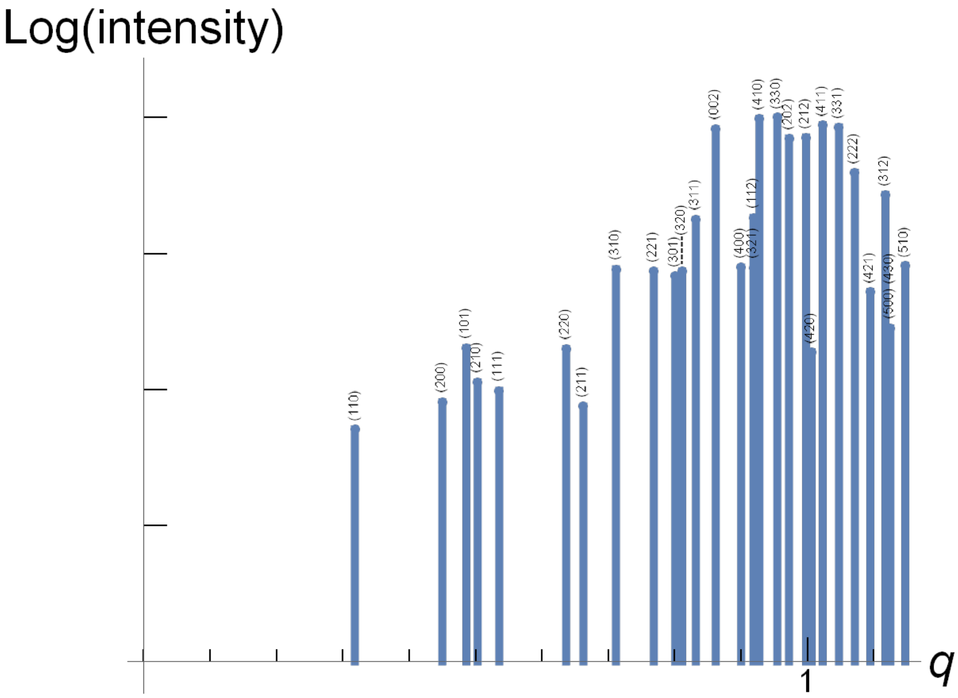

(b) σ phase (at $(\gamma = 1.08, \tau = -0.059)$).

Figure 3.5: Excess free energy plots with γ fixed. Free energy plot points are connected with straight lines.

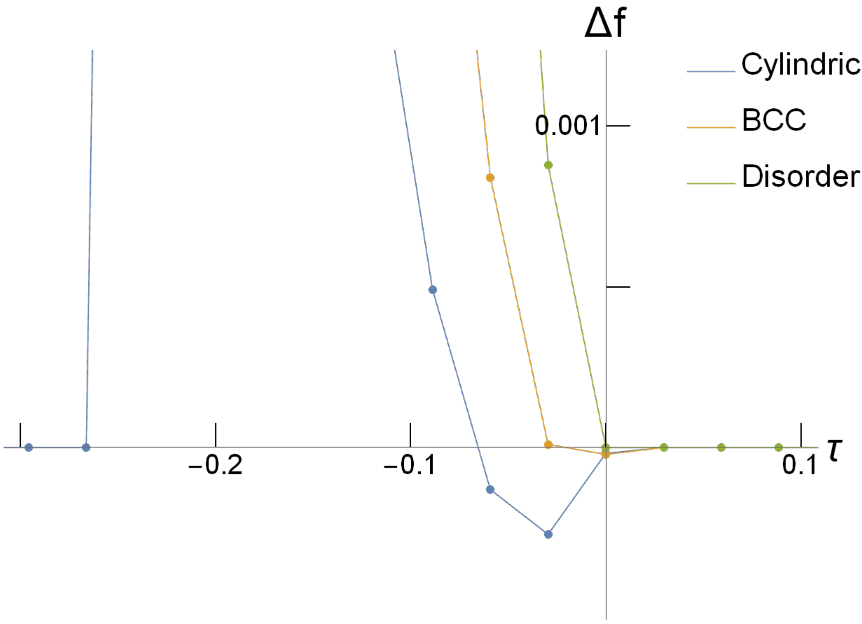

(a) Δf = ((free energy of indicated phase) − (free energy of lamellar phase)) *vs.* τ for $\gamma = 0.15$.

Figure 3.5: Excess free energy plots with γ fixed *cont.*

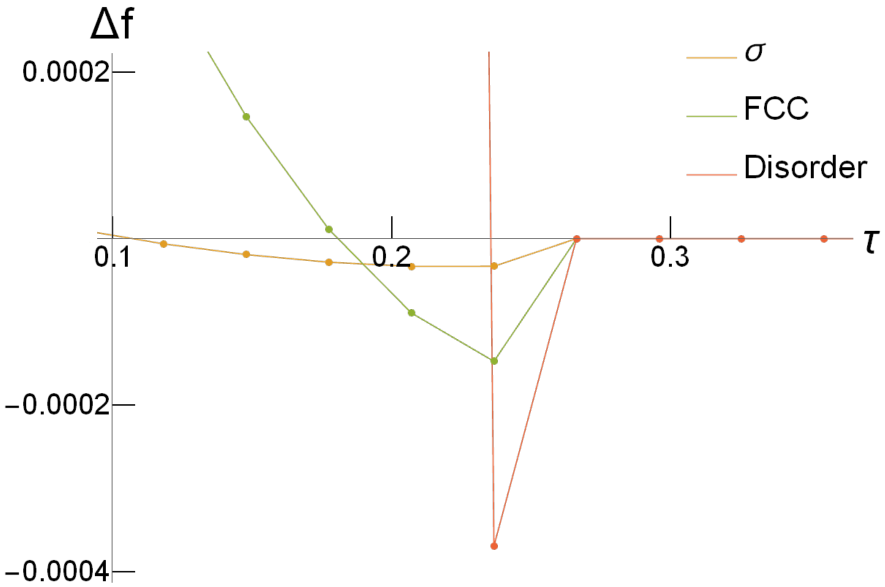

(b) Δf = ((free energy of indicated phase) − (free energy of A15 phase)) *vs.* τ for $\gamma = 1.23$.

Chapter 4

Discussion and Conclusion

4.1 Where do we go from Here?

We found that, when eight candidate phases (the disordered, cylindrical hexagonal, BCC, FCC, A15, σ, double gyroid, and lamellar phases) are considered, the σ and A15 phases have regions of stability within the Landau-Brazovskii phase diagram. This is despite the fact that the Landau-Brazovskii model is designed specifically for cases in which one wavelength dominates, and the σ and A15 phases have multiple characteristic length scales due to their complex unit cells with multiple nonequivalent lattice sites. Further research is required to better understand the reason for the emergence of the Frank-Kasper phases in such a simple model.

It would also be instructive to attempt to link the parameters in the Landau-Brazovskii model with physical parameters in soft matter systems which exhibit the σ and A15 phases. This has already been done [35, 37, 38] for linear diblock copolymers with equal Kuhn lengths, but it would be interesting to attempt such a derivation for systems such as liquid crystalline dendrimers [8, 9] and small ionic surfactants [6]. The derivation of the Landau-Brazovskii model for particular physical systems can be done by Taylor expanding the free energy functional in powers of the order parameter field and applying a mean field approximation, but this would yield a result that was valid only near the critical point. However, one might reasonably expect this type of derivation to produce a model which was qualitatively valid, to some extent, even far from the critical point.

Once a connection is made with a given physical system, this connection could be applied to the problem of identifying the origin of a universal phase transition sequence found in a number of soft matter systems. This sequence proceeds from the BCC to the σ to the A15 to the cylindrical hexagonal phase [7] as some parameter (such as the minority block fraction or temperature) is adjusted, and the sequence appears in a variety of soft matter systems, including block copolymers [14], small ionic surfactants [6], giant surfactants[1] [5], and dendrimers [9]. Hopefully, one could determine whether the Landau-Brazovskii model, when applied to these soft matter systems, exhibits a similar transition sequence.

Finally, it would be interesting to determine if other Frank-Kasper phases, not considered in this work, are stable in the phase diagram of the Landau-Brazovskii model. In particular, the Frank-Kasper C14 ($MgZn_2$) and C15

---

[1] In giant surfactants, a dodecagonal quasicrystalline phase can be observed in between the σ and A15 phases [5].

(Cu_2Mg) phases have been identified as stable or metastable structures in a number of soft matter systems, including diblock copolymers [29] and small ionic surfactants [27]. It would also be useful to determine whether dodecagonal quasicrystalline (DDQC) phases are stabilized by the Landau-Brazovskii model. Quasicrystalline phases are non-periodic phases which have been found in many metallic systems; they were originally discovered in Al-Mn alloys in the 1980s [53]. Quasicrystalline phases with 12-fold rotational symmetry (i.e., DDQCs) have also been discovered in a number of soft materials, including triblock [54] and tetrablock [15, 55] copolymers, binary systems of nanoparticles [56], giant surfactants [5], mesoporous silica [57], and colloids [58]. In some of these DDQC-forming systems [5, 15, 57], the σ and A15 phases can also be stabilized. Indeed, the σ and A15 phases are approximants to some DDQC phases [55, 59], and hence it would not be surprising if the Landau-Brazovskii model stabilizes DDQC structures.

4.2 Conclusion

The Landau-Brazovskii free energy functional is a generic model for studying weak first-order phase transitions in a near-isotropic system whose free energy is dominated by a single characteristic wavelength. We have shown that the phase behavior of this model depends only on two parameters, γ and τ in Eq. (1.3). We have, furthermore, shown that the Frank-Kasper σ and A15 phases, which have attracted recent interest due to their discovery in a wide variety of single-component soft condensed matter systems, are stable in the phase diagram of this model, at least when compared against the disordered, BCC, FCC, lamellar, double gyroid, and cylindrical hexagonal phases.

Our results provide some explanation for the appearence of the σ and A15 phases in such a wide array of soft matter systems: since the Landau-Brazovskii model is a very simple, generic, model (perhaps the simplest capable of generating ordered, periodic, phases), this discovery of the σ and A15 phases in its phase diagram suggests that the occurrence of these phases is a quite general feature of systems exhibiting periodic order, provided the right conditions are present. Such a conclusion is coincident with the existence of the σ and A15 phases in a range of soft matter systems, and the Landau-Brazovskii model would likely thus be a fruitful object for future study in this area.

Appendix A

σ and A15 Phase Data

A.1 A15 Structure

The A15 structure (space group: $Pm\overline{3}n$) consists of an eight-point basis on a simple cubic Bravais lattice. Let $\hat{\mathbf{x}}$, $\hat{\mathbf{y}}$, and $\hat{\mathbf{z}}$ be mutually perpendicular unit vectors in the directions of the three cubic axes, and let a be the lattice constant. $\hat{\mathbf{x}}$, $\hat{\mathbf{y}}$, and $\hat{\mathbf{z}}$ form a right-handed triple, such that $\hat{\mathbf{x}} \times \hat{\mathbf{y}} = \hat{\mathbf{z}}$. With this notation, the positions $\{\mathbf{r_i}\}$ of the basis atoms are as shown in Table A.1.

Table A.1: A15 basis coordinates and associated Wyckoff positions [21, 28].

Basis Atom Position	**Wyckoff Position**
$\mathbf{r_1} = \mathbf{0}$	2(a)
$\mathbf{r_2} = \frac{a}{2}\left(\hat{\mathbf{x}} + \hat{\mathbf{y}} + \hat{\mathbf{z}}\right)$	2(a)
$\mathbf{r_3} = a\left(\frac{1}{2}\hat{\mathbf{x}} + \frac{1}{4}\hat{\mathbf{z}}\right)$	6(c)
$\mathbf{r_4} = a\left(\frac{1}{2}\hat{\mathbf{x}} + \frac{3}{4}\hat{\mathbf{z}}\right)$	6(c)
$\mathbf{r_5} = a\left(\frac{1}{2}\hat{\mathbf{y}} + \frac{1}{4}\hat{\mathbf{x}}\right)$	6(c)
$\mathbf{r_6} = a\left(\frac{1}{2}\hat{\mathbf{y}} + \frac{3}{4}\hat{\mathbf{x}}\right)$	6(c)
$\mathbf{r_7} = a\left(\frac{1}{2}\hat{\mathbf{z}} + \frac{1}{4}\hat{\mathbf{y}}\right)$	6(c)
$\mathbf{r_8} = a\left(\frac{1}{2}\hat{\mathbf{z}} + \frac{3}{4}\hat{\mathbf{y}}\right)$	6(c)

A.2 σ Structure

The σ structure (space group: $P4_2/mnm$) is considerably more complicated than the A15 phase described above. Its underlying lattice is a primitive tetragonal Bravais lattice. Let $\hat{\mathbf{x}}$, $\hat{\mathbf{y}}$, and $\hat{\mathbf{z}}$ be mutually perpendicular unit vectors such that they form a right-handed triple where $\hat{\mathbf{x}} \times \hat{\mathbf{y}} = \hat{\mathbf{z}}$. Furthermore, let c be the length of the unit cell in the z-direction, and a the unit cell length in the x- and y- directions. A basis to the underlying tetragonal

Bravais lattice is thus given by $\{\mathbf{c}_1 = a\hat{\mathbf{x}}, \mathbf{c}_2 = a\hat{\mathbf{y}}, \mathbf{c}_3 = c\hat{\mathbf{z}}\}$, and the positions of the σ phase basis atoms are as shown in Table A.2.

Table A.2: σ basis coordinates and associated Wyckoff positions [28]. x_2, x_3, y_3, x_4, y_4, x_5, and z_5 are adjustable parameters.

Basis Atom Position	**Wyckoff Position**
$\mathbf{r_1} = \mathbf{0}$	2(a)
$\mathbf{r_2} = \frac{a}{2}\left(\hat{\mathbf{x}} + \hat{\mathbf{y}}\right) + \frac{c}{2}\hat{\mathbf{z}}$	2(a)
$\mathbf{r_3} = ax_2\left(\hat{\mathbf{x}} + \hat{\mathbf{y}}\right)$	4(f)
$\mathbf{r_4} = -ax_2\left(\hat{\mathbf{x}} + \hat{\mathbf{y}}\right)$	4(f)
$\mathbf{r_5} = a\left[\left(\frac{1}{2} - x_2\right)\hat{\mathbf{x}} + \left(\frac{1}{2} + x_2\right)\hat{\mathbf{y}}\right] + \frac{c}{2}\hat{\mathbf{z}}$	4(f)
$\mathbf{r_6} = a\left[\left(\frac{1}{2} - x_2\right)\hat{\mathbf{y}} + \left(\frac{1}{2} + x_2\right)\hat{\mathbf{x}}\right] + \frac{c}{2}\hat{\mathbf{z}}$	4(f)
$\mathbf{r_7} = a\left(x_3\hat{\mathbf{x}} + y_3\hat{\mathbf{y}}\right)$	8(i)
$\mathbf{r_8} = -a\left(x_3\hat{\mathbf{x}} + y_3\hat{\mathbf{y}}\right)$	8(i)
$\mathbf{r_9} = a\left(x_3\hat{\mathbf{y}} + y_3\hat{\mathbf{x}}\right)$	8(i)
$\mathbf{r_{10}} = -a\left(x_3\hat{\mathbf{y}} + y_3\hat{\mathbf{x}}\right)$	8(i)
$\mathbf{r_{11}} = a\left[\left(\frac{1}{2} - x_3\right)\hat{\mathbf{x}} + \left(\frac{1}{2} + y_3\right)\hat{\mathbf{y}}\right] + \frac{c}{2}\hat{\mathbf{z}}$	8(i)
$\mathbf{r_{12}} = a\left[\left(\frac{1}{2} + x_3\right)\hat{\mathbf{x}} + \left(\frac{1}{2} - y_3\right)\hat{\mathbf{y}}\right] + \frac{c}{2}\hat{\mathbf{z}}$	8(i)
$\mathbf{r_{13}} = a\left[\left(\frac{1}{2} - x_3\right)\hat{\mathbf{y}} + \left(\frac{1}{2} + y_3\right)\hat{\mathbf{x}}\right] + \frac{c}{2}\hat{\mathbf{z}}$	8(i)
$\mathbf{r_{14}} = a\left[\left(\frac{1}{2} + x_3\right)\hat{\mathbf{y}} + \left(\frac{1}{2} - y_3\right)\hat{\mathbf{x}}\right] + \frac{c}{2}\hat{\mathbf{z}}$	8(i)
$\mathbf{r_{15}} = a\left(x_4\hat{\mathbf{x}} + y_4\hat{\mathbf{y}}\right)$	8(i)$'$

Table A.2: σ basis coordinates and associated Wyckoff positions *cont.*

Basis Atom Position	**Wyckoff Position**
$\mathbf{r_{16}} = -a\left(x_4\hat{\mathbf{x}} + y_4\hat{\mathbf{y}}\right)$	8(i)′
$\mathbf{r_{17}} = a\left(x_4\hat{\mathbf{y}} + y_4\hat{\mathbf{x}}\right)$	8(i)′
$\mathbf{r_{18}} = -a\left(x_4\hat{\mathbf{y}} + y_4\hat{\mathbf{x}}\right)$	8(i)′
$\mathbf{r_{19}} = a\left[\left(\frac{1}{2} - x_4\right)\hat{\mathbf{x}} + \left(\frac{1}{2} + y_4\right)\hat{\mathbf{y}}\right] + \frac{c}{2}\hat{\mathbf{z}}$	8(i)′
$\mathbf{r_{20}} = a\left[\left(\frac{1}{2} + x_4\right)\hat{\mathbf{x}} + \left(\frac{1}{2} - y_4\right)\hat{\mathbf{y}}\right] + \frac{c}{2}\hat{\mathbf{z}}$	8(i)′
$\mathbf{r_{21}} = a\left[\left(\frac{1}{2} - x_4\right)\hat{\mathbf{y}} + \left(\frac{1}{2} + y_4\right)\hat{\mathbf{x}}\right] + \frac{c}{2}\hat{\mathbf{z}}$	8(i)′
$\mathbf{r_{22}} = a\left[\left(\frac{1}{2} + x_4\right)\hat{\mathbf{y}} + \left(\frac{1}{2} - y_4\right)\hat{\mathbf{x}}\right] + \frac{c}{2}\hat{\mathbf{z}}$	8(i)′
$\mathbf{r_{23}} = ax_5\left(\hat{\mathbf{x}} + \hat{\mathbf{y}}\right) + cz_5\hat{\mathbf{z}}$	8(j)
$\mathbf{r_{24}} = -ax_5\left(\hat{\mathbf{x}} + \hat{\mathbf{y}}\right) + cz_5\hat{\mathbf{z}}$	8(j)
$\mathbf{r_{25}} = ax_5\left(\hat{\mathbf{x}} + \hat{\mathbf{y}}\right) - cz_5\hat{\mathbf{z}}$	8(j)
$\mathbf{r_{26}} = -ax_5\left(\hat{\mathbf{x}} + \hat{\mathbf{y}}\right) - cz_5\hat{\mathbf{z}}$	8(j)
$\mathbf{r_{27}} = a\left[\left(\frac{1}{2} - x_5\right)\hat{\mathbf{x}} + \left(\frac{1}{2} + x_5\right)\hat{\mathbf{y}}\right] + (\frac{1}{2} + z_5)c\hat{\mathbf{z}}$	8(j)
$\mathbf{r_{28}} = a\left[\left(\frac{1}{2} + x_5\right)\hat{\mathbf{x}} + \left(\frac{1}{2} - x_5\right)\hat{\mathbf{y}}\right] + (\frac{1}{2} + z_5)c\hat{\mathbf{z}}$	8(j)
$\mathbf{r_{29}} = a\left[\left(\frac{1}{2} - x_5\right)\hat{\mathbf{x}} + \left(\frac{1}{2} + x_5\right)\hat{\mathbf{y}}\right] + (\frac{1}{2} - z_5)c\hat{\mathbf{z}}$	8(j)
$\mathbf{r_{30}} = a\left[\left(\frac{1}{2} + x_5\right)\hat{\mathbf{x}} + \left(\frac{1}{2} - x_5\right)\hat{\mathbf{y}}\right] + (\frac{1}{2} - z_5)c\hat{\mathbf{z}}$	8(j)

Appendix B

SAV Algorithm: A Brief Overview

The scalar auxiliary variable (SAV) algorithm, first introduced by Shen, Xu, and Yang [51, 52], provides a method for numerically solving a certain class of differential equations. In this appendix, I give the class of problems this algorithm is designed to solve, and give a summary of the algorithm and my implementation of it. Note that we mix our own notation with that of the creators of this algorithm [51]. Most of the notation should be familiar; I note only that I use the notation $\langle f|g\rangle = \int_{\Delta} fg \ \mathrm{d}x$ to denote the inner product.

B.1 Introduction

We roughly follow the presentation of the SAV algorithm given in [52]. Consider a functional $H\left[\phi\left(x\right)\right]$ of a scalar field $\phi\left(x\right)$. Assume that ϕ is subject to either periodic, or homogeneous von Neumann boundary conditions,[1] and let Δ be the domain over which ϕ is defined. Assume that ϕ obeys the following (pseudo)time evolution law:

$$\frac{\partial \phi}{\partial t} = \mathcal{G}\mu, \tag{B.1}$$

where t is a (pseudo)time parameter, $\mathcal{G}$ is a symmetric, negative semidefinite, linear operator (independent of ϕ), and:

$$\mu := \frac{\delta H}{\delta \phi} \tag{B.2}$$

is the variational derivative of H with respect to ϕ. Note that the negative semidefiniteness of $\mathcal{G}$ guarantees that H will be nonincreasing with increasing t. We wish to find $\phi(x;t)$ given $\phi(x;0)$ at some initial time $t = 0$. We will be interested in the steady state solution $\phi(x;t \to \infty)$ reached in the $t \to \infty$ limit, provided such a solution exists.

Let us suppose that H is bounded from below by a positive constant; that is, assume $H \geq C_0 > 0$. Furthermore, we assume that H can be split into a quadratic and a nonlinear part:

$$H = \frac{1}{2} \langle \phi | \mathcal{L}\phi \rangle + P[\phi], \tag{B.3}$$

---

[1] More specifically, according to the creators of the SAV algorithm, any boundary condition in which "all boundary terms will vanish when [integration] by parts [is] performed" [51] is valid.

where P can be nonlinear, and $\mathcal{L}$ is a linear, symmetric, positive semidefinite operator, independent of ϕ. P contains, we assume, only derivatives of lower order[2] than those in $\mathcal{L}$. Assume also that P is bounded from below by a positive constant; that is, suppose $P \geq C_1 > 0$.[3]

Eq. (B.1) can sometimes be difficult to solve with usual methods – if this equation is unstable, solving it by explicit iterative methods can be prohibitively expensive (for instance, by forcing an extremely small time step between iterations), and the implementation of implicit methods is also generally difficult to the nonlinearity of P. The SAV algorithm presents an alternate approach, which we found to work very well in practice.

B.2 Algorithm Details

We have given the assumptions underlying the SAV algorithm above, and we now turn to the algorithm itself. Again, we roughly follow the presentation in [51]. First, we introduce the "scalar auxilary variable" p:

$$p := \sqrt{P}. \tag{B.4}$$

Using Eqs. (B.1), (B.2), (B.3), and (B.4), we can rewrite the time evolution

---

[2] This condition on the derivatives in P is mentioned in [51], but that paper also suggests that only a weaker condition is necessary: the condition that P contains derivatives of lesser *or equal* order than/to the highest order derivatives in $\mathcal{L}$.

[3] We may also, without loss of generality, release the restriction on C_1 and allow it to be any real number, for in that case we may simply add a constant to P without changing the flow in Eq. (B.1).

of ϕ as follows:

$$\frac{\partial \phi}{\partial t} = \mathcal{G}\mu,$$

$$\mu = \mathcal{L}\phi + \frac{p}{\sqrt{P}}U, \tag{B.5}$$

$$\frac{\partial p}{\partial t} = \frac{1}{2\sqrt{P}} \int_{\Delta} U \frac{\partial \phi}{\partial t} \, \mathrm{d}x, \tag{B.6}$$

where

$$U[\phi] := \frac{\delta P}{\delta \phi} \tag{B.7}$$

is the variational derivative of P. One may then construct the first-order SAV algorithm by introducing the discrete time evolution law below:

$$\frac{\phi^{n+1} - \phi^n}{\Delta t} = \mathcal{G}\mu^{n+1}, \tag{B.8}$$

$$\mu^{n+1} = \mathcal{L}\phi^{n+1} + \frac{p^{n+1}}{\sqrt{P[\phi^n]}} U[\phi^n], \tag{B.9}$$

$$\frac{p^{n+1} - p^n}{\Delta t} = \frac{1}{2\sqrt{P[\phi^n]}} \int_{\Delta} U[\phi^n] \frac{\phi^{n+1} - \phi^n}{\Delta t} \, \mathrm{d}x, \tag{B.10}$$

$$p^0 = P[\phi^0], \tag{B.11}$$

where $\Delta t > 0$ is the time step, and where a superscript index k indicates a quantity associated with the kth iteration (that is, the quantity at time

$k\Delta t$, where $t = 0$ is the initial time) of the discrete time evolution scheme. By using the above first-order discretization scheme, together with an initial condition ϕ^0, we can approximate the time evolution of ϕ under Eq. (B.1). As explained in §2.4, we used this algorithm to minimize the Landau-Brazovskii free energy functional subject to the constraint that the zeroth moment of the density field is zero. In practice, we found this method to permit the use of much larger time increments Δt than, for instance, the more standard Euler or Runge-Kutta methods.

We may implement the first order SAV algorithm using the following three-step method, given in [51] (I have corrected one small typo):

1. Let ϕ^0 be the initial density profile. Define the following terms for iteration n:

   $$b^n := \frac{U[\phi^n]}{\sqrt{P[\phi^n]}}, \tag{B.12}$$

   and

   $$c^n := \phi^n + \Delta t p^n \mathcal{G} b^n - \frac{\Delta t}{2} \langle b^n | \phi^n \rangle \mathcal{G} b^n. \tag{B.13}$$

   Also define:

   $$\mathcal{A} = \mathcal{I} - \Delta t \mathcal{G} \mathcal{L}, \tag{B.14}$$

   where $\mathcal{I}$ is the identity operator. Compute b^n and c^n.

2. One can show that:

   $$\langle b^n | \phi^{n+1} \rangle = \frac{\langle b^n | \mathcal{A}^{-1} c^n \rangle}{1 - (\Delta t/2) \langle b^n | \mathcal{A}^{-1} \mathcal{G} b^n \rangle}, \tag{B.15}$$

   where $\mathcal{A}^{-1}$ is the inverse of $\mathcal{A}$. Compute $\langle b^n | \phi^{n+1} \rangle$.

3. One can also show that:

   $$\phi^{n+1} = \frac{\Delta t}{2} \left\langle b^n \middle| \phi^{n+1} \right\rangle \mathcal{A}^{-1}\mathcal{G}b^n + \mathcal{A}^{-1}c^n. \tag{B.16}$$

   Using this expression, compute ϕ^{n+1} using the results from the previous two steps.

4. Finally, update p using Eq. (B.10), which comes out to:

   $$p^{n+1} = p^n + \left\langle (b^n/2) \middle| \left(\phi^{n+1} - \phi^n\right) \right\rangle, \tag{B.17}$$

   noting that p^0 is defined by Eq. (B.11).

The only non-trivial parts of this algorithm involve the computation of the vector-inverse matrix products $\mathcal{A}^{-1}\mathcal{G}b^n$ and $\mathcal{A}^{-1}c^n$. If such products can be efficiently computed (as is the case in our implementation, as we work in a diagonal basis of $\mathcal{A}$), then the SAV algorithm has the potential to be highly efficient.

B.3 Implementation

Let us now consider our implementation of this algorithm. As discussed in §2.4, we used this algorithm to find steady-state ($t \to \infty$) solutions to Eq. (2.4). We reproduce Eq. (2.4) below:

$$\frac{\partial \psi}{\partial t} = \eta \nabla^2 \left[\frac{\delta f'}{\delta \psi}\right], \tag{B.18}$$

where f' is given by Eq. (2.1), which we likewise reproduce below:

$$f' = \frac{1}{V}\int_{\Delta} \mathrm{d}^3\mathbf{r} \left[\frac{(\xi')^2}{2}\left(\nabla^2\psi + \psi\right)^2 + \frac{\tau'}{2}\psi^2 - \frac{\gamma'}{3!}\psi^3 + \frac{1}{4!}\psi^4 \right] \tag{B.19}$$

ψ is defined with periodic boundary conditions over the unit cell domain Δ.

B.3.1 Construction of $\mathcal{L}$ and P

We will now split f' into a quadratic part $\frac{1}{2}\langle\psi|\mathcal{L}\psi\rangle$ and a nonlinear part $P[\psi]$. First, we make the following claim:

$$\int_{\Delta} \left(\nabla^2\psi + \psi\right)^2 \mathrm{d}^3\mathbf{r} = \int_{\Delta} \psi\left(\nabla^2 + 1\right)^2\psi \, \mathrm{d}^3\mathbf{r}, \tag{B.20}$$

where $\left(\nabla^2 + 1\right)^2\psi$ denotes the operator $(\nabla^2 + 1)$ applied twice to the field ψ. To prove this, recall the multidimensional integration-by-parts identity, as given in [60]:

$$\int_{\Omega} g\nabla\cdot\mathbf{f} \ \mathrm{d}V = -\int_{\Omega} \nabla g\cdot\mathbf{f} \ \mathrm{d}V + \int_{\partial\Omega} g\mathbf{f}\cdot\hat{\mathbf{n}} \ \mathrm{d}S,$$

where Ω denotes a region, $\partial\Omega$ its boundary, and $\hat{\mathbf{n}}$ a unit outward normal to $\partial\Omega$. Taking Ω to be our domain Δ, $\mathbf{f} = \nabla\left[\nabla^2\psi\right]$, and $g = \psi$, we have:

$$\begin{aligned}\int_{\Delta} \psi\nabla\cdot\nabla\left[\nabla^2\psi\right] \ \mathrm{d}^3\mathbf{r} &= \int_{\Delta} \psi\nabla^2\left[\nabla^2\psi\right] \ \mathrm{d}^3\mathbf{r} \\ &= -\int_{\Delta} \nabla\psi\cdot\nabla\left[\nabla^2\psi\right] \ \mathrm{d}^3\mathbf{r} + \int_{\partial\Delta} \psi\nabla\left[\nabla^2\psi\right]\cdot\hat{\mathbf{n}} \, \mathrm{d}^2\mathbf{r}.\end{aligned}$$

The surface integral vanishes because of the periodic boundary conditions, and we are left with:

$$\int_\Delta \psi \nabla^2 \left[\nabla^2 \psi\right] \, \mathrm{d}^3\mathbf{r} = -\int_\Delta \nabla\psi \cdot \nabla \left[\nabla^2\psi\right] \, \mathrm{d}^3\mathbf{r}.$$

However, the reader can easily verify that, for some function h, $\nabla \cdot [\nabla h \nabla^2 h] = \left(\nabla^2 h\right)^2 + \nabla h \cdot \nabla \left[\nabla^2 h\right]$ [60]. Making use of this identity, we can rewrite the equation above as:

$$\int_\Delta \psi \nabla^2 \left[\nabla^2 \psi\right] \, \mathrm{d}^3\mathbf{r} = \int_\Delta \left(\nabla^2\psi\right)^2 \mathrm{d}^3\mathbf{r} - \int_\Delta \nabla \cdot \left[\nabla\psi\nabla^2\psi\right] \, \mathrm{d}^3\mathbf{r}.$$

The second integral on the right-hand side can be evaluated as a surface integral using the divergence theorem, and it therefore vanishes by means of the periodic boundary conditions. Hence, we have the result:

$$\int_\Delta \psi \nabla^2 \left[\nabla^2 \psi\right] \, \mathrm{d}^3\mathbf{r} = \int_\Delta \left(\nabla^2\psi\right)^2 \mathrm{d}^3\mathbf{r}. \tag{B.21}$$

Using this result, the proof of Eq. (B.20) is trivial:

$$\begin{aligned}\int_\Delta \left(\nabla^2\psi + \psi\right)^2 \mathrm{d}^3\mathbf{r} &= \int_\Delta \mathrm{d}^3\mathbf{r} \left[\left(\nabla^2\psi\right)^2 + 2\psi\nabla^2\psi + \psi^2\right] \\ &= \int_\Delta \mathrm{d}^3\mathbf{r} \left[\psi\nabla^2\left[\nabla^2\psi\right] + 2\psi\nabla^2\psi + \psi^2\right] \\ &= \int_\Delta \psi\left(\nabla^2 + 1\right)^2\psi \, \mathrm{d}^3\mathbf{r}.\end{aligned}$$

Because of Eq. (B.20), we may now write Eq. (B.19) in the form:

$$f' = \frac{1}{2} \langle \psi | \mathcal{L} \psi \rangle + P[\psi],$$

where:

$$\mathcal{L} = (\xi')^2 (\nabla^2 + 1)^2, \tag{B.22}$$

and

$$P = \int_{\Delta} \mathrm{d}^3\mathbf{r} \left[\frac{\tau'}{2}\psi^2 - \frac{\gamma'}{3!}\psi^3 + \frac{1}{4!}\psi^4 \right]. \tag{B.23}$$

B.3.2 Computational Procedure

Now, we will consider the application of the SAV algorithm to solving Eq. (B.18), with our energy functional $H = f'$ (see Eq. (B.3)), $\phi = \psi$, $x = \mathbf{r}$, and P and $\mathcal{L}$ as given above. We will let η in Eq. (B.18) be 1, so that the operator $\mathcal{G}$ (see Eq. (B.1)) is ∇^2. From §B.1, we see that the necessary conditions for the use of the SAV algorithm are met: our boundary conditions are periodic, $\mathcal{L}$ is linear, symmetric, independent of ψ and positive semidefinite, $\mathcal{G}$ is negative semidefinite, symmetric, and independent of ψ, P is bounded from below due to its fourth-order term (we only need to add a constant to it to ensure it is bounded from below by a positive constant), and the quadratic term $\frac{1}{2} \langle \psi | \mathcal{L} \psi \rangle$ in f contains all of the highest order derivatives (P contains no derivatives).

We now turn to the computational procedure used to implement the SAV algorithm. Let $\{\psi^n(\mathbf{r}_{ijk})\}$ represent the discretized order parameter field at iteration n (see §2.4.2). Given an initial discretized order parameter field $\{\psi^0(\mathbf{r}_{ijk})\}$, our SAV algorithm implementation proceeds effectively as follows:

1. Compute the discrete Fourier transform (DFT; see §2.4.3) of $\{\psi^0(\mathbf{r}_{ijk})\}$, and call it $\left\{\hat{\psi}^0\left(\mathbf{q}_{\hat{i}\hat{j}\hat{k}}\right)\right\}$. We used the FFTW (Fastest Fourier Transform in the West) algorithm [61] to perform these transforms.
2. Estimate the quadratic part ($\frac{1}{2}\langle\psi|\mathcal{L}\psi\rangle$) of f' using the DFT computed in the previous step (the matrix elements of $\mathcal{L}$ are computed using Eq. (2.5)).
3. Use $\{\psi^0(\mathbf{r}_{ijk})\}$ to estimate $P[\psi^0]$, p^0, and the values $\{U[\psi^0(\mathbf{r}_{ijk})]\}$ of U on the grid used to discretize ψ. Add a constant α to our estimate of $P[\psi^0]$ to ensure a positive value for P.
4. Next, repeat the following steps until either the maximum iteration count is reached or the relative absolute free energy density difference between energies computed from subsequent iterations is reached:
    (a) Estimate $\langle b^n|\psi^n\rangle$ using Eq. (B.12) and the real space discretizations $\{\psi^0(\mathbf{r}_{ijk})\}$ and $\{U[\psi^0(\mathbf{r}_{ijk})]\}$.
    (b) Compute the DFT associated with b^n. Using this result and the results from the previous steps, compute the DFTs associated with $\mathcal{A}^{-1}c^n$ and $\mathcal{A}^{-1}\mathcal{G}b^n$ with Eqs. (B.14) and (B.13). This calculation is efficient since we are working in Fourier space, where we can use Eq. (2.5) to compute the matrix elements of $\mathcal{G}$ and $\mathcal{A}$ (these matrices will be diagonal in Fourier space, so, for instance, the inversion of $\mathcal{A}$ is trivial).

(c) Estimate $\langle b^n|\mathcal{A}^{-1}c^n\rangle$ and $\langle b^n|\mathcal{A}^{-1}\mathcal{G}b^n\rangle$ using the results from the previous step.

(d) Use the previous results to compute $\langle b^n|\phi^{n+1}\rangle$ from Eq. (B.15).

(e) Compute the DFT for ψ^{n+1}, $\left\{\hat{\psi}^{n+1}\left(\mathbf{q}_{\hat{i}\hat{j}\hat{k}}\right)\right\}$, using the previous results and Eq. (B.16). Perform an inverse DFT back to real space to get the real-space discretization of ψ^{n+1}.

(f) Using the previous results and Eq. (B.17), estimate p^{n+1}.

(g) Estimate the quadratic part of f', $\frac{1}{2}\langle\psi|\mathcal{L}\psi\rangle$, using the DFT for ψ^{n+1}, and estimate $P\left[\psi^{n+1}\right]$ and the real-space discretization of U for the next iteration (that is, $\{U\left[\psi^{n+1}\left(\mathbf{r}_{ijk}\right)\right]\}$) using the real space discretization of ψ^{n+1}. Add the constant α to the estimate of $P\left[\psi^{n+1}\right]$, as was done in step three.

Appendix C

Simulation Box Size Optimization Procedure

The minimization algorithm outlined in §2.4.4 includes the determination of the optimal simulation box width (W), length (L), and height (H), given the discrete Fourier transform (DFT) of the real-space discretization of the density profile. We outline here the procedure used to perform this optimization. We consider the case of a three-dimensional simulation box; however, the methods herein are easily applied to the one- and two-dimensional cases. Using the notation of §2.4.3, let us call the DFT $\left\{\hat{\psi}\left(\mathbf{q}_{\hat{i}\hat{j}\hat{k}}\right)\right\}$, where $\mathbf{q}_{\hat{i}\hat{j}\hat{k}} = \left(2\pi\hat{i}/W\right)\hat{\mathbf{x}} + \left(2\pi\hat{j}/L\right)\hat{\mathbf{y}} + \left(2\pi\hat{k}/H\right)\hat{\mathbf{z}}$. We wish to fix the Fourier components $\left\{\hat{\psi}\left(\mathbf{q}_{\hat{i}\hat{j}\hat{k}}\right)\right\}$, and minimize the free energy density f' with respect to W, L, and H. This amounts to minimizing f' by performing exclusively affine deformations of the density profile along the x, y, and z directions.

Let us define the quantities k_x, k_y, and k_z as follows:

$$k_x = \frac{2\pi}{W}, k_y = \frac{2\pi}{L}, k_z = \frac{2\pi}{H}. \tag{C.1}$$

Zhang and Zhang [41] demonstrate how one can determine the optimal k_x, k_y, and k_z. First, they define $\mathbf{b}_1$, $\mathbf{b}_2$, and $\mathbf{b}_3$ as primitive reciprocal lattice vectors of the Bravais lattice defined by the size and shape of the simulation box – if we fill space with identical copies of our simulation box, the corners of the simulation boxes will be points on a Bravais lattice, and a set of non-coplanar vectors formed from the edges of a simulation box will be a set of basis vectors for the lattice. Zhang and Zhang do not assume that the simulation box is a right rectangular prism, so $\mathbf{b}_1$, $\mathbf{b}_2$, and $\mathbf{b}_3$ can represent any Bravais lattice in their model. The optimal values for $\mathbf{b}_1$, $\mathbf{b}_2$, and $\mathbf{b}_3$ for the Landau-Brazovskii model can be determined, they show, by solving a system linear in $\mathbf{b}_1 \cdot \mathbf{b}_2$, $\mathbf{b}_2 \cdot \mathbf{b}_3$, $\mathbf{b}_3 \cdot \mathbf{b}_1$, ${b_1}^2$, ${b_2}^2$, and ${b_3}^2$. Since we are assuming that our simulation box is a right rectangular prism, the Bravais lattice defined by our simulation box is (in general) a simple orthorhombic lattice with mutually perpendicular basis vectors along the x, y, and z directions. The reciprocal lattice corresponding to this orthorhombic lattice is also orthorhombic, and we can set:

$$\mathbf{b_1} = k_x\hat{\mathbf{x}}, \mathbf{b_2} = k_y\hat{\mathbf{y}}, \mathbf{b_3} = k_z\hat{\mathbf{z}}. \tag{C.2}$$

Hence, the dot products between any two distinct vectors from the list above vanish. The linear system representing the optimality conditions for $\mathbf{b}_1$, $\mathbf{b}_2$, and $\mathbf{b}_3$ is given by Eqs. (2.9), (2.10), (2.11), (2.12), (2.13), and (2.14) in [41]. Eqs. (2.10), (2.11), and (2.13) in [41] represent the conditions for the minimization of the free energy density with respect to the dot products $\mathbf{b}_1 \cdot \mathbf{b}_2$,

$\mathbf{b}_2 \cdot \mathbf{b}_3$, $\mathbf{b}_3 \cdot \mathbf{b}_1$. Since these dot products are always zero in our case, we may ignore those equations. Hence, the conditions for the minimization of the free energy density f' with respect to k_x, k_y, and k_z are given by Eqs. (2.9), (2.12), and (2.14) in [41], where we used Eq. (C.2) and set the dot products $\mathbf{b}_i \cdot \mathbf{b}_j$, $i \neq j$ to zero:

$$\begin{aligned} {k_x}^2 \sum_{\hat{\imath},\hat{\jmath},\hat{k}} \left|\hat{\psi}\left(\mathbf{q}_{\hat{\imath}\hat{\jmath}\hat{k}}\right)\right|^2 \hat{\imath}^4 \;+\; {k_y}^2 \sum_{\hat{\imath},\hat{\jmath},\hat{k}} \left|\hat{\psi}\left(\mathbf{q}_{\hat{\imath}\hat{\jmath}\hat{k}}\right)\right|^2 \hat{\imath}^2\hat{\jmath}^2 \\ +\; {k_z}^2 \sum_{\hat{\imath},\hat{\jmath},\hat{k}} \left|\hat{\psi}\left(\mathbf{q}_{\hat{\imath}\hat{\jmath}\hat{k}}\right)\right|^2 \hat{\imath}^2\hat{k}^2 = \sum_{\hat{\imath},\hat{\jmath},\hat{k}} \left|\hat{\psi}\left(\mathbf{q}_{\hat{\imath}\hat{\jmath}\hat{k}}\right)\right|^2 \hat{\imath}^2, \end{aligned} \tag{C.3}$$

$$\begin{aligned} {k_x}^2 \sum_{\hat{\imath},\hat{\jmath},\hat{k}} \left|\hat{\psi}\left(\mathbf{q}_{\hat{\imath}\hat{\jmath}\hat{k}}\right)\right|^2 \hat{\imath}^2\hat{\jmath}^2 \;+\; {k_y}^2 \sum_{\hat{\imath},\hat{\jmath},\hat{k}} \left|\hat{\psi}\left(\mathbf{q}_{\hat{\imath}\hat{\jmath}\hat{k}}\right)\right|^2 \hat{\jmath}^4 \\ +\; {k_z}^2 \sum_{\hat{\imath},\hat{\jmath},\hat{k}} \left|\hat{\psi}\left(\mathbf{q}_{\hat{\imath}\hat{\jmath}\hat{k}}\right)\right|^2 \hat{\jmath}^2\hat{k}^2 = \sum_{\hat{\imath},\hat{\jmath},\hat{k}} \left|\hat{\psi}\left(\mathbf{q}_{\hat{\imath}\hat{\jmath}\hat{k}}\right)\right|^2 \hat{\jmath}^2, \end{aligned} \tag{C.4}$$

$$\begin{aligned} {k_x}^2 \sum_{\hat{\imath},\hat{\jmath},\hat{k}} \left|\hat{\psi}\left(\mathbf{q}_{\hat{\imath}\hat{\jmath}\hat{k}}\right)\right|^2 \hat{\imath}^2\hat{k}^2 \;+\; {k_y}^2 \sum_{\hat{\imath},\hat{\jmath},\hat{k}} \left|\hat{\psi}\left(\mathbf{q}_{\hat{\imath}\hat{\jmath}\hat{k}}\right)\right|^2 \hat{\jmath}^2\hat{k}^2 \\ +\; {k_z}^2 \sum_{\hat{\imath},\hat{\jmath},\hat{k}} \left|\hat{\psi}\left(\mathbf{q}_{\hat{\imath}\hat{\jmath}\hat{k}}\right)\right|^2 \hat{k}^4 = \sum_{\hat{\imath},\hat{\jmath},\hat{k}} \left|\hat{\psi}\left(\mathbf{q}_{\hat{\imath}\hat{\jmath}\hat{k}}\right)\right|^2 \hat{k}^2. \end{aligned} \tag{C.5}$$

These equations form a linear system in ${k_x}^2, {k_y}^2$, and ${k_z}^2$. After solving this system, the optimal box lengths can be determined using Eq. (C.1). My minimization program made use of the open source linear algebra library Eigen [62] to solve this system. In some cases, the equations above can have more than one solution: that is the case when the dimensionality of the structure considered is lower than the dimensionality of the simulation box. If this happens, it is an indication that the structure originally under consideration has decayed to another structure with lower dimensionality.

Appendix D

Phase Diagram Verification Methods

The Landau-Brazovskii phase diagram presented in Fig. 3.1 was created by comparing the free energy densities of a certain set of ordered phases. However, this phase diagram is not reliable if, at some points in one of the phase regions of the diagram, our minimization algorithm causes the supposedly stable phase to decay to some other phase, so that the free energy densities our algorithm associates with the stable phase in this region are actually the free energy densities of another phase.

To test for this, I examined the final minimized density profile of the supposedly stable phase for three sample points in each of the ordered phase regions we found in the Landau-Brazovskii phase diagram. In each case, I expected the density profile to match the structure of the ordered phase we predicted to be stable. To ensure this prediction was correct, I produced and visually analyzed plots produced from the final minimized density profile data. Some of these plots are shown in Fig. 3.3. I also ensured, for each of the non-lamellar[1] minimized density profiles I considered above, that the symmetry operations associated with the supposedly stable phase's space group were indeed symmetries of the minimized density profile (within a 10% tolerance). More precisely, I considered each symmetry operation within a generating set of all possible symmetry operations for that space group. For instance, let $\mathcal{O}$ be such an operation. Let ψ be an interpolation of final, minimized density profile data produced by our minimization algorithm, and let $\mathcal{O}\left[\psi\right]$ be the result of applying $\mathcal{O}$ to ψ. Also, let ψ_* be the maximum value of ψ. Then, I used numerical integration to ensure that $\frac{1}{V\psi_*}\int_\Delta \left|\psi\left(\mathbf{r}\right) - \mathcal{O}\left[\psi\left(\mathbf{r}\right)\right]\right| \mathrm{d}^n\mathbf{r} < 0.1$ was satisfied for all appropriate $\mathcal{O}$ ($n = 2$ for the cylindrical hexagonal phase, otherwise $n = 3$).

---

[1] The test described here is automatically satisfied for the lamellar phase, because of the periodic boundary conditions on ψ.

Appendix E

Additional Fourier-Space Final Density Profile Plots

In this section, we present additional Fourier-space plots derived from the density profile data used to generate the real-space plots in Chap. 3.

Figure E.1: Selected Fourier-space plots of final density profiles associated with the equilibrium phases in Fig. 3.1. On the y-axis is plotted $\log\left[\frac{\left\langle\left|\hat{\psi}_{\mathbf{q}}\right|^2\right\rangle_{|\mathbf{q}|=q}}{\max_{\mathbf{q}}\left(\left\langle\left|\hat{\psi}_{\mathbf{q}}\right|^2\right\rangle_{|\mathbf{q}|=q}\right)}\right]$. In other words, the y-axis variable is the logarithm of a scaled average of the square magnitudes of the Fourier components (that is, the components of the discrete Fourier transform) $\hat{\psi}_{\mathbf{q}}$ of ψ, where the average for a given q is over all $\mathbf{q}$ with magnitude q, and q is plotted on the x-axis. If the argument to the logarithm above is less than 10^{-7}, the associated peak is omitted from its plot. The indices above each peak represent sample Miller indices corresponding to the peak in question (in rare cases two or more such sample Miller indices are included).

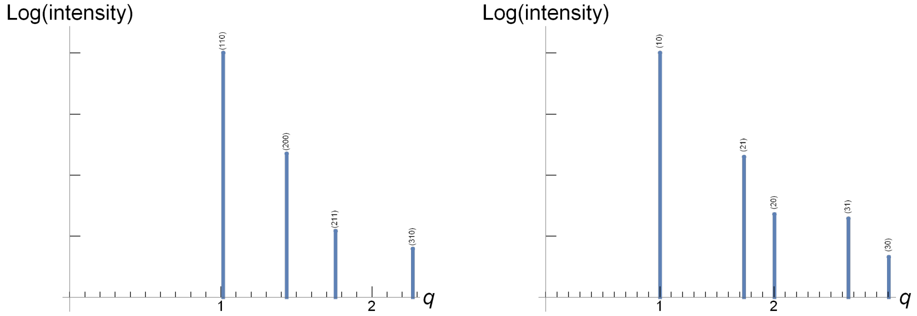

(a) BCC phase (at ($\gamma = 0.31, \tau = 0$)).

(b) Cylindrical hexagonal phase (at ($\gamma = 0.62, \tau = -0.12$)).

Figure E.1: Selected Fourier-space plots of final density profiles *cont.*

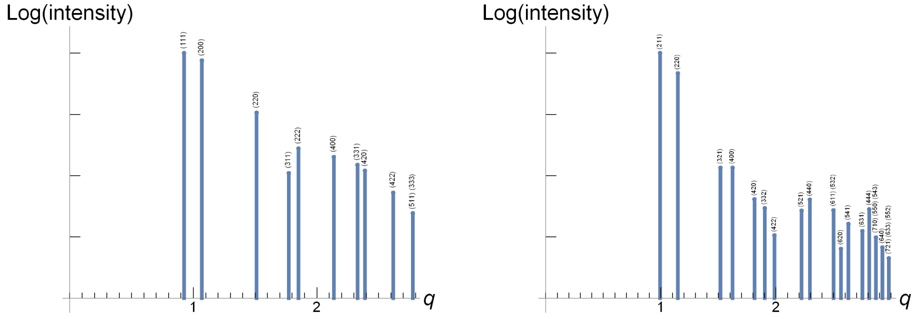

(c) FCC phase (at $(\gamma = 1.85, \tau = 0)$).

(d) Double gyroid phase (at $(\gamma = 0.46, \tau = -0.47)$).

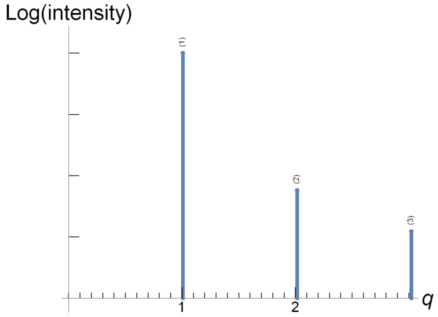

(e) Lamellar phase (at $(\gamma = 0.15, \tau = -0.24)$).

References

[1] J. van der Gucht, “Grand challenges in soft matter physics”, Front. Phys. **6**, 87 (2018).

[2] S. R. Nagel, “Experimental soft-matter science”, Rev. Mod. Phys. **89**, 025002 (2017).

[3] T. C. Lubensky, “Reflections on graduate education in soft matter”, Soft Matter **9**, 4948 (2013).

[4] A. Reddy, M. B. Buckley, A. Arora, F. S. Bates, K. D. Dorfman, and G. M. Grason, “Stable Frank-Kasper phases of self-assembled, soft matter spheres”, Proc. Natl. Acad. Sci. U.S.A. **115**, 10233 (2018).

[5] M. Huang, K. Yue, J. Wang, C.-H. Hsu, L. Wang, and S. Z. D. Cheng, “Frank-Kasper and related quasicrystal spherical phases in macromolecules”, Sci. China: Chem. **61**, 33 (2018).

[6] S. A. Kim, K.-J. Jeong, A. Yethiraj, and M. K. Mahanthappa, “Low-symmetry sphere packings of simple surfactant micelles induced by ionic sphericity”, Proc. Natl. Acad. Sci. U.S.A. **114**, 4072 (2017).

[7] W. Li, C. Duan, and A.-C. Shi, "Nonclassical spherical packing phases self-assembled from AB-type block copolymers", ACS Macro Lett. **6**, 1257 (2017).

[8] G. Ungar, Y. Liu, X. Zeng, V. Percec, and W.-D. Cho, "Giant supramolecular liquid crystal lattice", Science **299**, 1208 (2003).

[9] X. Zeng, G. Ungar, Y. Liu, G. Percec, A. E. Dulcey, and J. K. Hobbs, "Supramolecular dendritic liquid quasicrystals", Nature **428**, 157 (2004).

[10] V. S. K. Balagurusamy, G. Ungar, V. Percec, and G. Johansson, "Rational design of the first spherical supramolecular dendrimers self-organized in a novel thermotropic cubic liquid-crystalline phase and the determination of their shape by x-ray analysis", J. Am. Chem. Soc. **119**, 1539 (1997).

[11] S. Lee, M. J. Bluemle, and F. S. Bates, "Discovery of a Frank-Kasper sigma phase in sphere-forming block copolymer melts", Science **330**, 349 (2010).

[12] S. Lee, C. Leighton, and F. S. Bates, "Sphericity and symmetry breaking in the formation of Frank–Kasper phases from one component materials", Proc. Natl. Acad. Sci. U.S.A. **111**, 17723 (2014).

[13] K. Kim, A. Arora, R. M. Lewis III, M. Liu, W. Li, A.-C. Shi, K. D. Dorfman, and F. S. Bates, "Origins of low-symmetry phases in asymmetric diblock copolymer melts", Proc. Natl. Acad. Sci. U.S.A. **115**, 847 (2018).

[14] M. W. Bates et al., "Stability of the A15 phase in diblock copolymer melts", Proc. Natl. Acad. Sci. U.S.A. **116**, 13194 (2019).

[15] S. Chanpuriya et al., "Cornucopia of nanoscale ordered phases in sphere-forming tetrablock terpolymers", ACS Nano **10**, 4961 (2016).

[16] E. V. Shevchenko, D. V. Talapin, C. B. Murray, and S. O'Brien, "Structural characterization of self-assembled multifunctional binary nanoparticle superlattices", J. Am. Chem. Soc. **128**, 3620 (2006).

[17] F. C. Frank and J. S. Kasper, "Complex alloy structures regarded as sphere packings. I. Definitions and basic principles", Acta Crystallogr. **11**, 184 (1958).

[18] F. C. Frank and J. S. Kasper, "Complex alloy structures regarded as sphere packings. II. Analysis and classification of representative structures", Acta Crystallogr. **12**, 483 (1959).

[19] M. Liu, Y. Qiang, W. Li, F. Qiu, and A.-C. Shi, "Stabilizing the Frank-Kasper phases via binary blends of AB diblock copolymers", ACS Macro Lett. **5**, 1167 (2016).

[20] M. D. Sikirić, O. Delgado-Friedrichs, and M. Deza, "Space fullerenes: a computer search for new Frank-Kasper structures", Acta Crystallogr. **A66**, 602 (2010).

[21] A. K. Sinha, "Topologically close-packed structures of transition metal alloys", Prog. Mater. Sci. **15**, 81 (1972).

[22] T. S. Hales, "Cannonballs and honeycombs", Notices Am. Math. Soc. **47**, 440 (2000).

[23] G. M. Grason, *Frank Kasper phases of squishable spheres and optimal cell models*, J. Club Condens. Matter Phys. 2016.

[24] F. C. Frank, "Supercooling of liquids", Proc. Royal Soc. A **215**, 43 (1952).

[25] M. Huang, "Design, synthesis, and self-assembly of well-defined hybrid materials including polymer amphiphiles and giant tetrahedra molecules based on POSS nanoparticles", PhD thesis (University of Akron, 2015).

[26] A. Godeke, “A review of the properties of Nb_3Sn and their variation with A15 composition, morphology and strain state”, Supercond. Sci. Technol. **19**, R68 (2006).

[27] C. M. Baez-Cotto and M. K. Mahanthappa, “Micellar mimicry of intermetallic C14 and C15 Laves phases by aqueous lyotropic self-assembly”, ACS Nano **12**, 3226 (2018).

[28] M. J. Mehl, D. Hicks, C. Toher, O. Levy, R. M. Hanson, G. Hart, and S. Curtarolo, “The AFLOW library of crystallographic prototypes: part 1”, Comp. Mater. Sci. **136**, S1 (2017).

[29] K. Kim, M. W. Schulze, A. Arora, R. M. Lewis III, M. A. Hillmyer, K. D. Dorfman, and F. S. Bates, “Thermal processing of diblock copolymer melts mimics metallurgy”, Science **356**, 520 (2017).

[30] R. Lifshitz, “Explaining complex metals with polymers”, Proc. Natl. Acad. Sci. U.S.A. **111**, 17698 (2014).

[31] Y. Gao, H. Deng, W. Li, and F. Qiu, “Formation of nonclassical ordered phases of AB-type multiarm block copolymers”, Phys. Rev. Lett. **116**, 068304 (2016).

[32] N. Xie, W. Li, F. Qiu, and A.-C. Shi, “σ phase formed in conformationally asymmetric AB-type block copolymers”, ACS Macro Lett. **3**, 906 (2014).

[33] S. A. Brazovskii, “Phase transition of an isotropic system to a nonuniform state”, Sov. Phys. — JETP **41**, 85 (1975).

[34] E. I. Kats, V. V. Lebedev, and A. R. Muratov, “Weak crystallization theory”, Phys. Rep. **228**, 1 (1993).

[35] G. H. Fredrickson and E. Helfand, “Fluctuation effects in the theory of microphase separation in block copolymers”, J. Chem. Phys. **87**, 697 (1987).

[36] A.-C. Shi, “Nature of anisotropic fluctuation modes in ordered systems”, J. Phys.: Condens. Matter **11**, 10183 (1999).

[37] L. Leibler, “Theory of microphase separation in block copolymers”, Macromolecules **13**, 1602 (1980).

[38] T. Ohta and K. Kawasaki, “Equilibrium morphology of block copolymer melts”, Macromolecules **19**, 2621 (1986).

[39] A. Ciach, J. Pekalski, and W. T. Gozdz, “Origin of similarity of phase diagrams in amphiphilic and colloidal systems with competing interactions”, Soft Matter **9**, 6301 (2013).

[40] M. Seul and D. Andelman, “Domain shapes and patterns: the phenomenology of modulated phases”, Science **267**, 476 (1995).

[41] P. Zhang and X. Zhang, “An efficient numerical method of Landau–Brazovskii model”, J. Comput. Phys. **227**, 5859 (2008).

[42] C. A. Lambert, L. H. Radzilowski, and E. L. Thomas, “Triply periodic level surfaces as models for cubic tricontinuous block copolymer morphologies”, Phil. Trans. Royal Soc. A **354**, 2009 (1996).

[43] R. M. Kaufmann, S. Khlebnikov, and B. Wehefritz-Kaufmann, “The geometry of the double gyroid wire network: quantum and classical”, J. Noncommut. Geom. **6**, 623 (2012).

[44] R. A. Wickham and A.-C. Shi, “Nucleation of stable cylinders from a metastable lamellar phase in a diblock copolymer melt”, J. Chem. Phys. **118**, 10293 (2003).

[45] M. W. Matsen, "Cylinder↔sphere epitaxial transitions in block copolymer melts", J. Chem. Phys. **114**, 8165 (2001).

[46] M. J. Park, J. Bang, T. Harada, K. Char, and T. P. Lodge, "Epitaxial transitions among FCC, HCP, BCC, and cylinder phases in a block copolymer solution", Macromolecules **37**, 9064 (2004).

[47] Y. Rancon and J. Charvolin, "Epitaxial relationships during phase transformations in a lyotropic liquid crystal", J. Phys. Chem. **92**, 2646 (1988).

[48] T. Honda and T. Kawakatsu, "Epitaxial transition from gyroid to cylinder in a diblock copolymer melt", Macromolecules **39**, 2340 (2006).

[49] J.-C. Crivello, R. Souques, A. Breidi, and J.-M. Joubert, *ZenGen: a tool to generate ordered configurations for systematic DFT calculations*, Online [`http://zengen.cnrs.fr/manual.pdf`], 2015.

[50] K. Yue et al., "Geometry induced sequence of nanoscale Frank–Kasper and quasicrystal mesophases in giant surfactants", Proc. Natl. Acad. Sci. U.S.A. **113**, 14195 (2016).

[51] J. Shen, J. Xu, and J. Yang, *A new class of efficient and robust energy stable schemes for gradient flows*, arXiv:1710.01331, 2017.

[52] J. Shen, J. Xu, and J. Yang, "The scalar auxiliary variable (SAV) approach for gradient flows", J. Comput. Phys. **353**, 407 (2018).

[53] D. Shechtman, I. Blech, D. Gratias, and J. W. Cahn, "Metallic phase with long-range orientational order and no translational symmetry", Phys. Rev. Lett. **53**, 1951 (1984).

[54] K. Hayashida, T. Dotera, A. Takano, and Y. Matsushita, "Polymeric quasicrystal: mesoscopic quasicrystalline tiling in ABC star polymers", Phys. Rev. Lett. **98**, 195502 (2007).

[55] J. Zhang and F. S. Bates, "Dodecagonal quasicrystalline morphology in a poly(styrene-b-isoprene-b-styrene-b-ethylene oxide) tetrablock terpolymer", J. Am. Chem. Soc. **134**, 7636 (2012).

[56] D. V. Talapin, E. V. Shevchenko, M. I. Bodnarchuk, X. Ye, J. Chen, and C. B. Murray, "Quasicrystalline order in self-assembled binary nanoparticle superlattices", Nature **461**, 964 (2009).

[57] C. Xiao, N. Fujita, K. Miyasaka, Y. Sakamoto, and O. Terasaki, "Dodecagonal tiling in mesoporous silica", Nature **487**, 349 (2012).

[58] S. Fischer, A. Exner, K. Zielske, J. Perlich, S. Deloudi, W. Steurer, P. Lindner, and S. Forster, "Colloidal quasicrystals with 12-fold and 18-fold diffraction symmetry", Proc. Natl. Acad. Sci. U.S.A. **108**, 1810 (2011).

[59] C. R. Iacovella, A. S. Keys, and S. C. Glotzer, "Self-assembly of soft-matter quasicrystals and their approximants", Proc. Natl. Acad. Sci. U.S.A. **108**, 20935 (2011).

[60] R. C. Rogers, *The calculus of several variables*, Online [`http://www.math.nagoya-u.ac.jp/~richard/teaching/s2016/Ref2.pdf`], 2011.

[61] M. Frigo and S. G. Johnson, "The design and implementation of FFTW3", in Proceedings of the IEEE (2005), pp. 216–231.

[62] G. Guennebaud and B. Jacob et al., *Eigen v3*, `http://eigen.tuxfamily.org`, 2010.